Monthly Notices
of the
ROYAL ASTRONOMICAL SOCIETY

MNRAS **459,** 3377–3394 (2016)
Advance Access publication 2016 April 21

doi:10.1093/mnras/stw899

Forming supermassive black hole seeds under the influence of a nearby anisotropic multifrequency source

John A. Regan,[1,2]★ Peter H. Johansson[2] and John H. Wise[3]

[1] *Institute for Computational Cosmology, Durham University, South Road, Durham DH1 3LE, UK*
[2] *Department of Physics, University of Helsinki, Gustaf Hällströmin katu 2a, FI-00014 Helsinki, Finland*
[3] *Center for Relativistic Astrophysics, Georgia Institute of Technology, 837 State Street, Atlanta, GA 30332, USA*

Accepted 2016 April 14. Received 2016 April 14; in original form 2015 November 2

ABSTRACT

The photodissociation of H_2 by a nearby anisotropic source of radiation is seen as a critical component in creating an environment in which a direct collapse black hole may form. Employing radiative transfer we model the effect of multifrequency (0.76–60 eV) radiation on a collapsing halo at high redshift. We vary both the shape of the spectrum which emits the radiation and the distance to the emitting galaxy. We use blackbody spectra with temperatures of $T = 10^4$ K and 10^5 K and a realistic stellar spectrum. We find that an optimal zone exists between 1 and 4 kpc from the emitting galaxy. If the halo resides too close to the emitting galaxy the photoionizing radiation creates a large H II region which effectively disrupts the collapsing halo, too far from the source and the radiation flux drops below the level of the expected background and the H_2 fraction remains too high. When the emitting galaxy is initially placed between 1 and 2 kpc from the collapsing halo, with a spectral shape consistent with a star-forming high-redshift galaxy, then a large central core forms. The mass of the central core is between 5000 and 10 000 $M_\odot$ at a temperature of approximately 1000 K. This core is however surrounded by a reservoir of hotter gas at approximately 8000 K, which leads to mass inflow rates of the order of $\sim 0.1\ M_\odot\ yr^{-1}$.

Key words: methods: numerical – cosmology: theory.

1 INTRODUCTION

The discovery of a significant number of quasars (∼40) at redshifts greater than six hosting black holes with masses exceeding $\gtrsim 10^9\ M_\odot$(Fan et al. 2006; Mortlock et al. 2011; Venemans et al. 2013; Wu et al. 2015) has challenged our understanding of how supermassive black holes (SMBHs) can form. The most straightforward mechanism is to assume that SMBHs grow through accretion and possibly mergers of remnant black holes from Population III (Pop III) collapse at the end of their rather short lifetimes. However, this argument suffers from numerous obstacles, with the prime issue being a time-scale argument. The growth by spherical accretion of a black hole is governed by the Eddington limit

$$M(t) = M(t_0)\exp\left(\frac{1-\epsilon}{\epsilon}\frac{t}{t_{\rm edd}}\right), \tag{1}$$

where ϵ is the radiative efficiency, $M(t)$ is the mass at time t and $t_{\rm edd}$ is the Eddington time, $t_{\rm edd}$ is approximately 450 Myr taking $\epsilon = 0.1$. Therefore, a stellar mass black hole forming at 500 Myr has of the order of 10 or so e-folding times to reach a mass of $10^9\ M_\odot$, where the growth is due to radiatively efficient accretion on to the black hole. This, coupled with the fact that the initial mass function of the first stars is hotly debated (Stacy, Greif & Bromm 2010; Clark et al. 2011; Greif et al. 2011; Bromm 2013; Hirano et al. 2014) and that subsequent accretion on to the first stellar mass black holes is likely to be inefficient (Johnson & Bromm 2007; Alvarez, Wise & Abel 2009; Milosavljević, Couch & Bromm 2009; Hosokawa et al. 2011) makes this mechanism for forming early SMBHs unattractive and difficult to reconcile with current observations of SMBHs at high redshift.

The direct collapse mechanism circumvents the above limitations to some extent by forming large seed black holes making growth to supermassive size by a redshift of six achievable. The pathway to producing a large seed is currently unclear with numerous avenues under investigation (Bromm & Loeb 2003; Wise, Turk & Abel 2008; Regan & Haehnelt 2009a,b; Tseliakhovich & Hirata 2010; Inayoshi & Omukai 2012; Agarwal et al. 2013; Latif et al. 2013; Agarwal et al. 2014; Regan, Johansson & Haehnelt 2014a; Tanaka & Li 2014; Inayoshi, Visbal & Kashiyama 2015; Mayer et al. 2015). Regardless of the final outcome, the direct collapse mechanism requires that the gas cloud that eventually collapses to form a massive black hole seed is hotter than the gas cloud that produces the first stars. The increased temperature elevates the Jeans mass, thus allowing a

---

★ E-mail: john.a.regan@durham.ac.uk

Published by Oxford University Press on behalf of the Royal Astronomical Society

larger object to initially form. In order to keep the temperature of the gas high, cooling must be somehow disrupted. Assuming the gas to be metal-free, this means that the availability of H_2 must be reduced. This can be achieved either through photodissociation or collisional dissociation.

Collisional dissociation of H_2 ($H_2 + H \rightarrow 3\,H$) is effective for gas of a primordial composition and high temperature satisfying the criteria of the 'zone of no-return' (Visbal, Haiman & Bryan 2014a). Inayoshi & Omukai (2012) suggested that cold accretion shocks may provide a pathway to collisionally dissociate H_2 during gravitational collapse; however, Fernandez et al. (2014) demonstrated, through numerical simulations, that in the absence of a photodissociating background, this method is difficult to achieve in practice as the collisional processes tend to operate at the virial radius and not in the centre of the halo.

Photodissociation of H_2 has been studied by several authors as a viable means of disrupting H_2 cooling at high redshift where metal cooling is unavailable (Omukai 2001; Oh & Haiman 2002; Bromm & Loeb 2003; Shang, Bryan & Haiman 2010; Latif et al. 2014a,b, 2015). In this case, radiation in the Lyman–Werner (LW) band with energies between 11.2 and 13.6 eV is able to dissociate H_2 via the two step Solomon process (Field, Somerville & Dressler 1966; Stecher & Williams 1967). The process operates by exciting the molecule from the electronic ground state, $X^1\Sigma_g^+$, to the $B^1\Sigma_u^+$ or $C^1\Gamma_u$ state. These are the Lyman and Werner states of H_2. The subsequent decay to the ground state then leads to the dissociation of the molecule in 15 per cent of cases. The Solomon process can therefore be written as

$$H_2 + \gamma \rightarrow H_2^* \tag{2}$$

$$H_2^* \rightarrow H + H + \gamma. \tag{3}$$

Lower energy radiation can also influence the H_2 abundances by photodetaching the intermediary ion H^-. The primary route to H_2 formation is through the reaction

$$H + H^- \rightarrow H_2 + e^-. \tag{4}$$

Therefore, by photodetaching the electron from the H^- ion, the formation rate of H_2 is severely compromised.

$$H^- + \gamma \rightarrow H + e^-, \tag{5}$$

where the photodetachment threshold is approximately 0.76 eV. Radiation in the infrared band is therefore very effective at destroying the intermediary required for H_2 formation. Finally, H_2^+ is also an intermediary for forming H_2.

$$H_2^+ + H \rightarrow H_2^* + H^+. \tag{6}$$

H_2^+ is destroyed by radiation between approximately 0.1 and 25 eV (Stancil 1994).

$$H_2^+ + \gamma \rightarrow H + H^+. \tag{7}$$

Numerous studies have been undertaken to uncover the flux required to disrupt H_2 formation to the extent that a large central object can form within a halo cooled predominantly by atomic hydrogen (e.g. Omukai 2001; Shang et al. 2010; Wolcott-Green et al. 2011) with the general consensus being that an intensity of approximately 1000 J_{21}[1] is required for radiation with a blackbody spectrum of 10^5 K, with an intensity of closer to 100 J_{21} required for radiation with a blackbody spectrum of 10^4 K. However, more recent studies have called into question the appropriateness of assuming a blackbody spectrum (Sugimura, Omukai & Inoue 2014; Agarwal & Khochfar 2015), when instead, a more realistic spectral energy distribution (SED) is what is required. Agarwal et al. (2016) has also noted that trying to determine a single value of $J_{\rm crit}$ is likely to be very difficult given the dependence of $J_{\rm crit}$ on the distance to the nearby radiation source(s), and its spectral shape and evolution. Furthermore, as discussed by Latif & Volonteri (2015), an isothermal collapse is not necessarily required to form a supermassive star and subsequently a direct collapse black hole (DCBH). In this case, then finding a single value of $J_{\rm crit}$ becomes even more challenging.

Rather the focus should centre on modelling the direct collapse under realistic cosmological conditions. Using the results from high-resolution simulations of the early universe and using them to determine a realistic SED turns earlier approaches on their heads. Instead of trying to determine a value for the intensity, J, we should model the effect realistic sources can have and study the viability of the direct collapse model under realistic cosmological conditions as found in the very early universe.

In this work, we focus on the key component of an anisotropic source. Building on the work of (Regan, Johansson & Wise 2014b, hereafter R14), we evaluate the collapse of a high-redshift gas cloud under the influence of a nearby anisotropic source. We have included radiation from 0.76 eV up to 60 eV allowing us to probe the impact from a much more realistic radiation source. This is in comparison to R14, where only the effects of radiation in the LW band were included. Furthermore, we have updated our chemical model based on the work of Glover (2015a). We model the irradiating source as a blackbody with effective temperatures of $T_{\rm eff} = 10^4$ K and 10^5 K and also using a realistic SED generated using the stellar population synthesis models of Bruzual & Charlot (2003). The parameters for creating the SED is based on the SFRs and stellar masses found in the 'Renaissance Simulations' of Chen et al. (2014). We have imposed a cutoff at energies greater than 60 eV in this study, thus ignoring the effects of X-rays in this case. The effects (both positive and negative) of X-ray radiation have been examined by Inayoshi & Omukai (2011) and Inayoshi & Tanaka (2015) and Latif et al. (2015). We will also examine this important component in an upcoming study (Regan, Johansson & Wise 2016) but this study focuses solely on the effects of the stellar component.

The paper is laid out as follows: in Section 2, we describe the numerical approach used including the halo setup, the chemical model and radiation prescription employed; in Section 3, we describe the results of our numerical simulations; in Section 4, we discuss the importance of the results, and in Section 5, we present our conclusions. Throughout this paper, we assume a standard Λcold dark matter cosmology with the following parameters (Planck Collaboration XVI 2014, based on the latest Planck data), $\Omega_{\Lambda,0} = 0.6817$, $\Omega_{\rm m,0} = 0.3183$, $\Omega_{\rm b,0} = 0.0463$, $\sigma_8 = 0.8347$ and $h = 0.6704$. We further assume a spectral index for the primordial density fluctuations of $n = 0.9616$.

2 NUMERICAL SETUP

We have used the publicly available adaptive mesh refinement (AMR) code ENZO (Bryan et al. 2014).[2] In particular, we use

---

[1] J_{21} is defined as 10^{-21} erg cm^{-2} s^{-1} Hz^{-1} sr^{-1}.

[2] http://enzo-project.org/

version 3.0[3] which is the bleeding edge version of the code incorporating a range of new features. We created a fork off the 3.0 mainline and included improved support for radiative transfer based on the Moray implementation of Wise & Abel (2011) and chemical modelling using the `Grackle` library.

All simulations are run within a box of 1 h^{-1} Mpc (comoving), the root grid size is 256^3 and we employ three levels of nested grids. The grid nesting and initial conditions are created using MUSIC (Hahn & Abel 2011). Within the most refined region (i.e. level 3), the dark matter particle mass is $\sim$103 $\mathrm{M}_{\odot}$. In order to increase further the dark matter resolution of our simulations, we split the dark matter particles according to the prescription of Kitsionas & Whitworth (2002) and as described in Regan, Johansson & Wise (2015). We split particles centred on the position of the final collapse as found from lower resolution simulations within a region with a comoving side length of 43.75 h^{-1} kpc. Each particle is split into 13 daughter particles resulting in a final high-resolution region with a dark matter particle mass of $\sim$8 $\mathrm{M}_{\odot}$. The particle splitting is done at a redshift of 40 well before the collapse of the target halo. Convergence testing to study the impact of lower dark matter particle masses on the physical results was conducted and is discussed in Section 2.4.

The baryon resolution is set by the size of the grid cells, in the highest resolution region, this corresponds to approximately 0.48 h^{-1} kpc comoving (before adaptive refinement). The maximum refinement level for all of the simulations was set to 16. Refinement is triggered in ENZO when the refinement criteria are exceeded. The refinement criteria used in this work were based on three physical measurements: (1) the dark matter particle overdensity, (2) the baryon overdensity and (3) the Jeans length. The first two criteria introduce additional meshes when the overdensity ($\frac{\Delta\rho}{\rho_{\rm mean}}$) of a grid cell with respect to the mean density exceeds 8.0 for baryons and/or DM. Furthermore, we set the *MinimumMassForRefinementExponent* parameter to -0.1 making the simulation super-Lagrangian and therefore reducing the threshold for refinement as higher densities are reached. For the final criteria, we set the number of cells per Jeans length to be 16 in these runs.

2.1 Ray tracing

We enhanced the radiative transfer algorithm by upgrading the maximum HEALPIX (Górski et al. 2005) level to 29. This allows for the ray-tracing algorithm to penetrate even the densest grid structure created by the AMR framework within ENZO. Without including this modification, the ray tracer is unable to properly resolve the most highly refined regions produced by ENZO's adaptive refinement mechanisms. The angular resolution of the ray-tracing algorithm is determined by the number of pixels that the HEALPIX routines create as the rays propagate outwards. The angular resolution is given by

$$\omega = \sqrt{\frac{4\pi}{N_{\rm pix}}}, \tag{8}$$

where ω is the angular resolution in steradians and $N_{\rm pix}$ is the number of pixels created by the HEALPIX solver. The number of pixels is given by

$$N_{\rm pix} = 12 * 4^l, \tag{9}$$

where l is the level of pixelization. Using 64-bit numerical resolution, l can reach a maximum value of 29. As the rays propagate through the simulation, they split when the associated solid angle is greater than $1/\kappa$ times the area of the cell that the ray is traversing, where κ is the number of rays per cell. In our simulations, we set κ to 5.1 (see Wise & Abel 2011 for more details on this parameter) which is the default value. l increases to allow the rays to split and the resolution of the ray tracer can always match the resolution of the AMR cells.

The ray-tracing solver in ENZO-3.0 is able to model the ionization of H, He and He^+. It can also account for the photodissociation of H_2 for photons with energies within the LW band. We have added further frequency channels to the ray-tracing solver including H^- photodetachment and H_2^+ dissociation to complement the already existing algorithms. The ray tracer is therefore able to properly account for all of the relevant photoionizations and photodissociations relevant for studying the direct collapse mechanism. Similarly to R14, we employ the self-shielding model of Wolcott-Green et al. (2011) when calculating the H_2 dissociation rate.[4]

2.2 Chemical modelling

We adopt here the 26 reaction network determined by Glover (2015a) as the most appropriate network for solving the chemical equations required by the direct collapse model in a gas of primordial composition with no metal pollution. The network consists of 10 individual species: H, H^+, He, He^+, He^{++}, e^-, H_2, H_2^+ $\mathrm{H}^-$and HeH^+. Additionally, we included a further seven reactions which accounts for the recombinations (4) and photoionizations (3) of H, He, and He^+ which occurs when the elements are photoionized due to photon energies greater than 13.6, 25.4 and 54.4 eV, respectively.

To implement the chemical network we have extensively modified the open source code `Grackle-2.1`[5,6] (Bryan et al. 2014; Kim et al. 2014). `Grackle-2.1`self-consistently solves the 33 set reaction network including photoionizations. The network includes the most up-to-date rates as described in Glover & Jappsen (2007), Glover & Abel (2008), Glover & Savin (2009), Coppola et al. (2011), Coppola et al. (2012), Glover (2015a), Glover (2015b) and Latif et al. (2015). The reaction network is described in full in Table 1. The gas is allowed to cool radiatively during the simulation and this is also accounted for using the `Grackle-2.1` module. Here, the rates have again been updated to account for recent updates in the literature (Glover 2015a). The cooling mechanisms included in the model are collisional excitation cooling, collisional ionization cooling, recombination cooling, bremsstrahlung and Compton cooling off the cosmic microwave background.

2.3 Models

For this study, we analyse a single halo. The halo studied is identical to one used in Regan et al. (2015) with the initial conditions created with the MUSIC code. The central idea is to place a radiating source close to a collapsing halo and investigate the effect of a realistic radiation field on the collapse of the halo and to determine

---

[3] Changeset: 7f49adb4c9b4

[4] We also ran simulations where we modelled the dissociation of H_2 by a direct calculation of the optical depth [i.e. Dissociation Rate $\propto \exp(-N_{\mathrm{H}_2}\sigma_{\mathrm{H}_2})$], in this case, we found very similar results with the temperature in the central regions of the collapsed halo being lower on average by about 300 K.

[5] https://grackle.readthedocs.org/

[6] Changeset: 88143fb25480

Table 1. Reaction network.

No.	Reaction	Notes	Reference
1.	$\mathrm{H + e \rightarrow H^+ + 2e}$	–	1, 2
2.	$\mathrm{H^+ + e \rightarrow H + \gamma}$	Case B recombination	1, 3
3.	$\mathrm{He + e \rightarrow He^+ + \gamma}$	–	1, 2
4.	$\mathrm{He^+ + e \rightarrow He + \gamma}$	Effective He$^+$ recombination rate*	1, 4
5.	$\mathrm{He^+ + e \rightarrow He^{++} + 2e}$	–	5
6.	$\mathrm{He^{++} + e \rightarrow He^+ + \gamma}$	Case B recombination	5
7.	$\mathrm{H + e \rightarrow H^- + \gamma}$	–	1, 6
8.	$\mathrm{H^- + H \rightarrow H_2 + e}$	–	7, 8
9.	$\mathrm{H + H^+ \rightarrow H_2^+ + \gamma}$	–	7, 9, 10
10.	$\mathrm{H_2^+ + H \rightarrow H_2 + H^+}$	–	1, 11
11.	$\mathrm{H_2 + H^+ \rightarrow H_2^+ + H}$	–	1, 12
12.	$\mathrm{H_2 + H \rightarrow 3H}$	–	7, 13
13.	$\mathrm{H^- + e \rightarrow H + 2e}$	–	1, 2
14.	$\mathrm{H^- + H \rightarrow 2H + e}$	–	1, 2
15.	$\mathrm{H^- + H^+ \rightarrow 2H}$	–	1, 14
16.	$\mathrm{H^- + H^+ \rightarrow H_2^+ + e}$	–	1, 15
17.	$\mathrm{H_2^+ + e \rightarrow 2H}$	–	5, 7, 10, 16
18.	$\mathrm{H + H + H \rightarrow H + H_2}$	–	7, 17
19.	$\mathrm{H + H \rightarrow H + H^+ + e}$	–	7, 18, 19
20.	$\mathrm{H + He \rightarrow H^+ + He + e}$	–	7, 20
21.	$\mathrm{H_2^+ + H \rightarrow H^+ + H + H}$	–	7, 10, 20
22.	$\mathrm{H_2^+ + He \rightarrow HeH^+ + H}$	–	1, 21
23.	$\mathrm{H_2 + He \rightarrow H + H + He}$	–	1, 22, 23
24.	$\mathrm{HeH^+ + H \rightarrow H_2^+ + He}$	–	1, 24
25.	$\mathrm{H^- + He \rightarrow H + He + e}$	–	1
26.	$\mathrm{He + H^+ \rightarrow HeH^+ + \gamma}$	–	1, 25
27.	$\mathrm{HeH^+ + e \rightarrow He + H}$	–	1, 26
28.	$\mathrm{H_2 + \gamma \rightarrow H + H}$	Use fitting function from Wolcott-Green, Haiman & Bryan (2011)	
29.	$\mathrm{H^- + \gamma \rightarrow H + e}$	Photodetachment	27
30.	$\mathrm{H_2^+ + \gamma \rightarrow H + H^+}$	Photodissociation	28
31.	$\mathrm{H + \gamma \rightarrow H^+ + e}$	Hydrogen ionization	
32.	$\mathrm{He + \gamma \rightarrow He^+ + e}$	Helium ionization	
33.	$\mathrm{He^+ + \gamma \rightarrow He^{++} + e}$	Double Helium ionization	

Notes. The 33 species reaction network used in our modified version of `Grackle-2.1`. References: (1) Glover & Savin (2009), (2) Janev, Langer & Evans (1987), (3) Ferland et al. (1992), (4) Hummer & Storey (1998), (5) Abel et al. (1997), (6) Wishart (1979), (7) Glover (2015a), (8) Kreckel et al. (2010), (9) Latif et al. (2015), (10) Coppola et al. (2011), (11) Karpas, Anicich & Huntress (1979), (12) Savin et al. (2004), (13) Martin, Schwarz & Mandy (1996), (14) Croft, Dickinson & Gadea (1999), (15) Poulaert et al. (1978), (16) Schneider et al. (1994), (17) Forrey (2013), (18) Lenzuni et al. (1991), (19) Omukai (2000), (20) Krstić & Janev (2003), (21) Black (1981), (22) Dove et al. (1987), (23) Walkauskas & Kaufman 1975, (24) Linder et al. (1995), (25) Juřek, Špirko & Kraemer 1995, (26) Guberman (1994), (27) Tegmark et al. (1997), (28) Stancil (1994). *This is a linear combination of Case A, Case B and Dielectric contributions as described in Glover & Savin (2009).

the viability of the direct collapse method. The idea that close-by neighbours are required for direct collapse has previously been studied analytically by Dijkstra et al. (2008), Dijkstra, Ferrara & Mesinger (2014) and more recently using synchronized halo pairs by Visbal, Haiman & Bryan (2014b). For each simulation, we vary the source characteristics (SED) and the distance of the source to the maximum density point. In each case, the simulation is initialized at $z = 99$ and evolved until a redshift of 40.0. At this point, the pre-galactic cloud has started to assemble but has not yet reached a mass that supports PopIII star formation. Continuing to evolve the simulation at this point would result in the formation of a Pop III star at a redshift of $z \approx 33$ (see Ctrl simulation in Table 2). We now select the point of maximum density at $z = 40$ and place a single radiation particle at a distance of 0.5, 1 and 2 kpc resulting in three different simulations. Further models are defined for the stellar spectrum case with initial distances of 4.0, 8.0 and 12.0 kpc. The flux from the source is identical in each case and only the SED and distance from the point of maximum density changes in each case. The specification of the radiation particles are listed in Table 2 resulting in a total of 13 different models.

2.4 Dark matter convergence

In order to evaluate the extent to which convergence is achieved in our simulations, we follow the study undertaken by Regan et al. (2015). Their rule of thumb for dark matter resolution in simulations of high-redshift collapse states that

$$\frac{M_{\mathrm{core}}}{M_{\mathrm{DM,part}}} > 100.0, \tag{10}$$

where M_{core} is the baryonic mass within the core[7] of the halo and $M_{\mathrm{DM,\,part}}$ is the dark matter particle mass (equivalent to the dark matter mass resolution). In Table 2, the core mass of the halo is displayed in the final column. As noted above, our dark matter mass resolution for all of our simulations is $\sim 8\ \mathrm{M_{\odot}}$. We have performed simulations at lower resolution and found that the resulting

---

[7] The core of the halo is defined at the point where the baryonic mass exceeds the dark matter mass. This fluctuates between approximately 1 and 5 pc across the simulations. We therefore choose 1 pc to define the radius of the core of the halo in all cases for consistency.

Table 2. Radiation source.

Sim name	Init. dist. (kpc)	Spectrum	z_{coll}	Final dist. (kpc)	T_{vir} (K)	M_{200} ($\mathrm{M}_{\odot}$)	M_{core} ($\mathrm{M}_{\odot}$)
Ctrl	–	–	$z = 32.18$	–	1784	1.12×10^6	2010
05-T4	0.5	BB ($T = 10^4$ K)	$z = 30.08$	0.8	3129	2.90×10^6	5625
1-T4	1.0	BB ($T = 10^4$ K)	$z = 30.86$	1.4	2282	1.73×10^6	3686
2-T4	2.0	BB ($T = 10^4$ K)	$z = 31.63$	2.6	2003	1.37×10^6	2633
05-T5	0.5	BB ($T = 10^5$ K)	$z = 21.50$	5.0	9152	2.34×10^7	3494
1-T5	1.0	BB ($T = 10^5$ K)	$z = 22.81$	5.3	8003	1.75×10^7	3537
2-T5	2.0	BB ($T = 10^5$ K)	$z = 29.17$	2.8	3844	4.10×10^6	8132
05-SSED	0.5	Stellar SED	$z = 21.70$	4.9	10721	2.92×10^7	6146
1-SSED	1.0	Stellar SED	$z = 25.25$	1.9	6224	1.04×10^7	9476
2-SSED	2.0	Stellar SED	$z = 28.67$	2.9	4225	4.84×10^6	7269
4-SSED	4.0	Stellar SED	$z = 29.97$	5.4	3181	2.96×10^6	6117
8-SSED	8.0	Stellar SED	$z = 30.87$	10.4	2276	1.71×10^6	3889
12-SSED	12.0	Stellar SED	$z = 31.44$	15.2	2162	1.55×10^6	3243

Notes. Each model is run with the radiation source at an initial distance from the centre of the collapsing halo of 0.5, 1.0 and 2.0 kpc (physical). The initial distance is the distance at $z = 40$. For each of these models, the spectrum is varied between a blackbody spectrum with an effective temperature of $T = 10^4$ K (BB1e4) and $T = 10^5$ K (BB1e5) and a stellar SED (maximum photon energy = 60 eV). Further simulations with the source placed at distances of 4.0, 8.0 and 12.0 kpc are run for the stellar spectrum only. Finally, a control simulation (Ctrl) is run with no radiation field present. All distances are in physical kpc unless explicitly stated. The core mass in the final column denotes the baryonic mass inside a 1 pc radius around the densest point.

differences in the thermal history of the model are negligible and are confident that we have achieved convergence for this resolution scale.

2.5 Radiation source

The radiation source is a point particle. It is massless and is fixed in comoving space. The physical distance between the source and the collapsing halo therefore inevitably increases due to the expansion of the universe at this redshift. The source of radiation is placed at a distance of between 0.5 and 12 kpc, depending on the given model being tested, from the point of maximum density at a redshift of 40. In each case, we use a luminosity of 1.2×10^{52} photons s^{-1} (above the H^- photodetachment energy of 0.76 eV) that originates from a galaxy with a stellar mass of 10^3 $\mathrm{M}_{\odot}$ at $z = 40$. The galaxy has a specific star formation rate (SFR) of sSFR = 40 Gyr^{-1} resulting in a stellar mass of 10^5 $\mathrm{M}_{\odot}$ at $z = 20$. The stellar mass at $z = 20$ and the specific SFR are consistent with the largest galaxies prior to reionization in the Renaissance Simulations of Chen et al. (2014). We then calculate its spectrum with the Bruzual & Charlot (2003) models with a metallicity of 10^{-2} $\mathrm{Z}_{\odot}$ and compute the photon luminosity from it. The spectrum does not include emission from the nebular component and is solely due to stellar emission.

As stated in the Introduction, J_{21} is the standard unit used to measure radiation (background) intensities. It is a measure of the intrinsic brightness or intensity of a source which is assumed to be constant at all points in space. We therefore also quote this value to be consistent with the literature noting, however, that in all cases, our radiation is from a single direction and not constant at all points. To calculate the intensity, J, in units of J_{21}, we sum the contributions to J from each energy bin used in our model and normalize J at the hydrogen ionization edge as follows

$$J' = \sum_{E,i} \frac{k_i E}{4\pi^2 \sigma_i(E)} \tag{11}$$

$$J = \frac{J'}{\nu_{\mathrm{H}} J_{21}}, \tag{12}$$

where J' is the sum of the intensities for each species, i, over all energy bins, E. Here k_i is the number of photoionizations (or dissociations) per second for species i, $\sigma_i(E)$ is the cross-section for species i at energy E. Finally, ν_{H} is the frequency at the hydrogen ionization edge. The extra factor of π in the denominator accounts for the solid angle. J is now the intensity of the radiation background in units of J_{21}. Individual contributions to the intensity are summed and normalized at the hydrogen edge, the normalization of individual contributions follows the same procedure described elsewhere in the literature (e.g. Haiman, Abel & Rees 2000). By summing over the individual contributions to the intensity and normalizing at the hydrogen edge, we are able to display a single, well defined, value for the intensity at all points as a function of distance from our source. Note that this definition of the mean intensity differs somewhat from those used in previous studies of DCBH formation where a background intensity is used. Care should be taken when comparing our values of J with the values quoted in these studies as ours are due to an anisotropic multifrequency radiation source.

In this study, we make use of three different methods to control the SED of the source. We use a blackbody spectrum with an effective temperature of $T = 10^4$ K and one with $T = 10^5$ K consistent with previous studies of dissociating H_2 (Shang et al. 2010; Latif et al. 2015). In order to account for energy in different radiation bands, we use a seven-bin model to probe the effect of radiation with different energies. As such, we select radiative transfer bins with energy of 0.76, 8.0, 12.8, 14.79, 20.46, 27.62 and 60 eV. The final energy bin is artificially cut just above the double ionization threshold of Helium (54.42 eV). We will investigate the effects of X-ray radiation, with energies greater than 60 eV, in a follow-up paper. The first three energy bins are weighted by the cross-section peaks for H^-, H_2^+ and H_2 photodetachment/dissociation, respectively. The final four energy bins are determined using the `sedop` code developed by Mirocha et al. (2012) which determines the optimum number of energy bins needed to accurately model radiation with energy above the ionization threshold of hydrogen. For computational reasons, we do not include more than seven energy bins in this study as the ray tracer scales with the number of energy bins used and the simulations would quickly become computationally too demanding.

Furthermore, we do not attempt to take into account any sources of background radiation in our model. At these redshifts ($z \gtrsim 20$), the background flux in the LW is likely to be very small (Dijkstra

Table 3. Radiation SED.

Spectrum	Energy bins (eV)	Photon fraction (PF)
No extinction		
Blackbody ($T = 10^4$ K)	0.76, 8.0, 12.8	0.9746, 0.0252, 0.0002
Blackbody ($T = 10^5$ K)	0.76, 8.0, 12.8, 14.79, 20.46, 27.62, 60.0	0.0795, 0.1440, 0.0745, 0.0741, 0.2484, 0.1124, 0.2671
Stellar	0.76, 8.0, 12.8, 14.79, 20.46, 27.62, 60.0	0.4130, 0.3170. 0.1080, 0.414, 0.0399, 0.0324, 0.0278
With xtinction		
Blackbody ($T = 10^4$ K)	0.76, 8.0, 12.8	0.9746, 0.0252, 0.0002
Blackbody ($T = 10^5$ K)	0.76, 8.0, 12.8, 14.79, 20.46, 27.62, 60.0	0.0795, 0.1440, 0.0745, 2.36e-07, 1.38e-03, 1.21e-02, 0.2122
Stellar	0.76, 8.0, 12.8, 14.79, 20.46, 27.62, 60.0	0.4130, 0.3170, 0.1080, 1.32e-07, 2.23e-04, 3.49e-03, 2.26e-02

Notes. The energy bins and the fractional number of photons are given for each spectrum used in this study. The photon fractions are given for the cases with and without extinction from the host galaxy ISM. The fractions without extinction are not used in this study but are included for reference for the reader. The blackbody spectrum with an effective temperature of $T = 10^4$ K has no photons with energies greater than the ionization threshold of hydrogen (13.6 eV) due to the exponential drop in the spectrum at energies greater than approximately 1 eV. In contrast, the $T = 10^5$ K blackbody spectrum peaks at energies greater than the ionizational threshold of hydrogen. The stellar spectrum has a more even distribution with a tilt towards energies in the infrared and optical.

et al. 2008; Johnson, Greif & Bromm 2008) and instead we require a nearby source to provide a strong, local, dissociating flux.

2.6 Sampling the energy spectrum

The energies and fractional number of photons in each energy bin for all three models are shown in Table 3. During test runs, we found that it was necessary to include a method to model the extinction properties of the interstellar medium (ISM) of the source galaxy. Without extinction, the hydrogen ionizing radiation created an unrealistically large H II region around the radiation source. In order to increase the realism of our simulations, we instead adopted a simple model of ISM extinction. The model convolves the spectral energies from our three fiducial spectra with a simple modelling of the optical depth to ionizing radiation as follows

$$\mathrm{PF_{ext}(E) = PF(E) \times \exp(-\sigma(E_{ph}) \times N(H\,I)_{avg})}, \tag{13}$$

where PF(E) is the photon fraction at the energy, E, $\mathrm{PF_{ext}(E)}$ is the photon fraction when the extinction is accounted for, σ(E) is the cross-section of hydrogen at that energy and $\mathrm{N(H\,I)_{avg}}$ is the column density of hydrogen averaged over the source galaxy. For our model, we choose an average value of $\mathrm{N(H\,I)_{avg}}$ of $2.5 \times 10^{18}\ \mathrm{cm^{-2}}$ consistent with the results from the simulations of Wise & Cen (2009). Physically, this is motivated by the fact that low-density channels of neutral hydrogen allow for the escape of ionizing radiation between approximately 13.6 and 50 eV from the radiating galaxy. These channels are somewhat transient and evolve over time (Wise et al. 2014) meaning that over a sufficient amount of time (approximately 80 Myr), the halo receiving the flux is swept over by ionizing radiation in these bands rather than being illuminated constantly. Our ISM modelling is an attempt to take this effect into account. In Table 3, we therefore include the photon fraction both with and without the extinction factor, so that the reader can easily see the differences. The extinction factor is set to 1.0 for energy below the ionization threshold of neutral hydrogen, thus having no effect in that case. The mean free path of photons below the ionization threshold of hydrogen is comparatively long and is not included in our model. Strong internal LW flux will dissociate most of the H_2 in the source galaxy with the exception of some molecular clouds, which have a small geometric cross-section and can be safely ignored. We only employ the photon fractions which include the extinction factor in our production runs (i.e. the bottom three lines).

The spectrum in the case of the $T = 10^4$ K blackbody is strongly tilted towards radiation with energy in the optical and infrared. The exponential fall-off in the number of photons with energies greater than a few electron volts means that there are virtually no photons capable of ionizing hydrogen with this spectrum. For the blackbody spectrum with $T = 10^5$ K, the peak in the SED is shifted towards higher energies and in this case, the photons are capable of ionizing hydrogen and helium. The spectrum based on a stellar SED is more evenly distributed but with a clear tilt towards lower energy photons. A plot of each spectrum is shown in Figs 1 and 2.

In the left-hand panel of Fig. 1, we have plotted the spectrum for the 10^4 K blackbody spectrum. Energy in eV is plotted on the x-axis while the number of photons emitted per second is plotted on the y-axis. For the case of the 10^4 K spectrum, the peak in the SED occurs at between 1 and a few eV in the infrared part of the spectrum and most photons are emitted with this energy. No photons with energies greater than the ionization threshold of hydrogen are emitted in our model for this spectrum. In the right-hand panel of Fig. 1, we have made the same plot for the 10^5 K blackbody spectrum. In this case, the effect of the extinction factor is clearly evident. The extinction manifests itself as a sharp drop in the photon count at energies greater than 13.6 eV before eventually recovering as the cross-section to hydrogen falls off to higher energies. The gap in the spectrum accounts for absorptions by the ISM. It should also be noted that in this case, the sum of the fractions does not equate to unity ($0.08 + 0.15 + 0.08 + 0.22 = 0.53 \neq 1.0$). These fractions are passed to the ray tracer via a parameter file and as a result the number of hydrogen ionizing photons is strongly reduced in cases where extinction is included.

In the left-hand panel of Fig. 2, we show the SED for the case of the stellar spectrum and in the right-hand panel, we show the photon number count versus energy. The stellar spectrum peaks in the UV with a significant fraction of the photons contributing to the direct dissociation of H_2 via the Solomon process. As well as this, there is a substantial fraction of photons which contribute towards photodetaching. The two intermediary species H^- and H_2^+. The fraction of hydrogen ionizing photons in the stellar SED is significantly lower than the 10^5 K spectrum but none the less non-zero and so a H II region will be forming around the source and overtime will expand. The values of the individual energies of each energy bin are available in Table 3.

3 RESULTS

Each of the models described in Table 2 result in a qualitatively different result. The difference in the initial distance to the source and the SED of that source mean that the collapse of the nearby

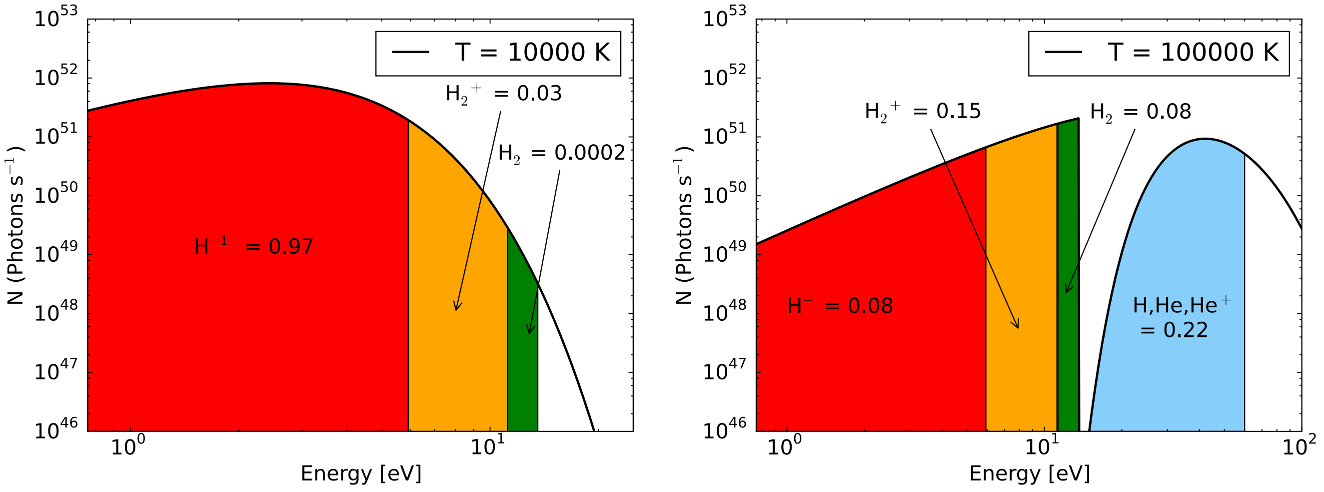

Figure 1. The left-hand panel shows the blackbody spectrum with an effective temperature of 10^4 K. The fractional number of photons which effects each species is shown (or pointed to with an arrow) for each species. The right-hand panel shows the blackbody spectrum when the effective temperature is 10^5 K. In this case, the spectrum includes photons which can ionize hydrogen and helium. The 10^5 K spectrum also includes the extinction factor due to absorption from the ISM which we include in our models. The absorption of ionizing photons causes the large gap in the spectrum around 13.6 eV.

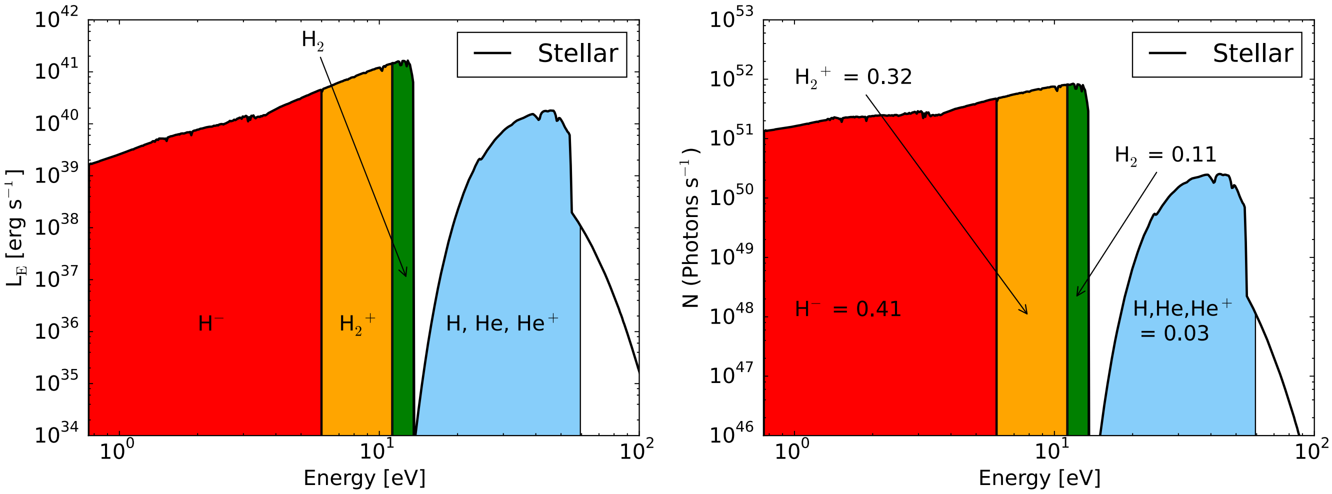

Figure 2. The left-hand panel shows the luminosity from a stellar spectrum extracted from the Renaissance Simulation of Chen et al. (2014). The total stellar mass of the spectrum is 1×10^5 $M_\odot$ at $z = 20$. As with the blackbody spectrum of 10^5 K, we employ an extinction factor for photons with energy greater than 13.6 eV and a cutoff for photons greater than 60 eV. In the right-hand panel, we plot the same spectrum with the photon luminosity (in units of photons per second) on the y-axis. The fraction of photons in each energy band is indicated. For the case of the stellar spectrum, most of the photons are lower energy photons with energies less than 13.6 eV.

halo is either significantly delayed or else the collapse is prevented entirely and a different halo collapses (i.e. one that is further from the source). We will now discuss the impact of each spectrum type (BB1e4, BB1e5 and stellar SED) on the target halo. We will begin by looking at the visual impact of the radiation fields before looking more quantitatively at the impact of the radiation.

3.1 Visual inspections

3.1.1 *Blackbody with $T = 10^4$ K (BB1e4)*

In Figs 3–5, we show projections for all models where the initial distance is 0.5, 1.0 or 2.0 kpc. We mark the source with a white circle, the point of maximum density with a black circle and the target halo with a red circle. The target halo is only marked in the cases where it does not overlap with the point of maximum density (i.e. in simulations where the radiation from the source disrupts entirely the target halo). The distance from the source to the collapse halo is identified in each case. As we will see, the target halo is not always the halo which collapses first. Looking first at Fig. 3 where we plot the visualization for the realizations with a blackbody spectrum of $T = 10^4$ K (BB1e4), the target halo and collapse halo are the same halo. The distances from the source to the target halo changes with time due to cosmic expansion and the evolution of the system (the source is fixed in comoving space). The collapse shifts to lower redshifts as the source is brought closer to the target halo due to the increased dissociation of H_2 from the radiation source. However, in each case, the overall morphology of the system remains unchanged. Note also that in each of these cases, the final virial temperature of the halo remains well below the atomic cooling threshold indicating that the dominant coolant remains H_2 in all of the cases.

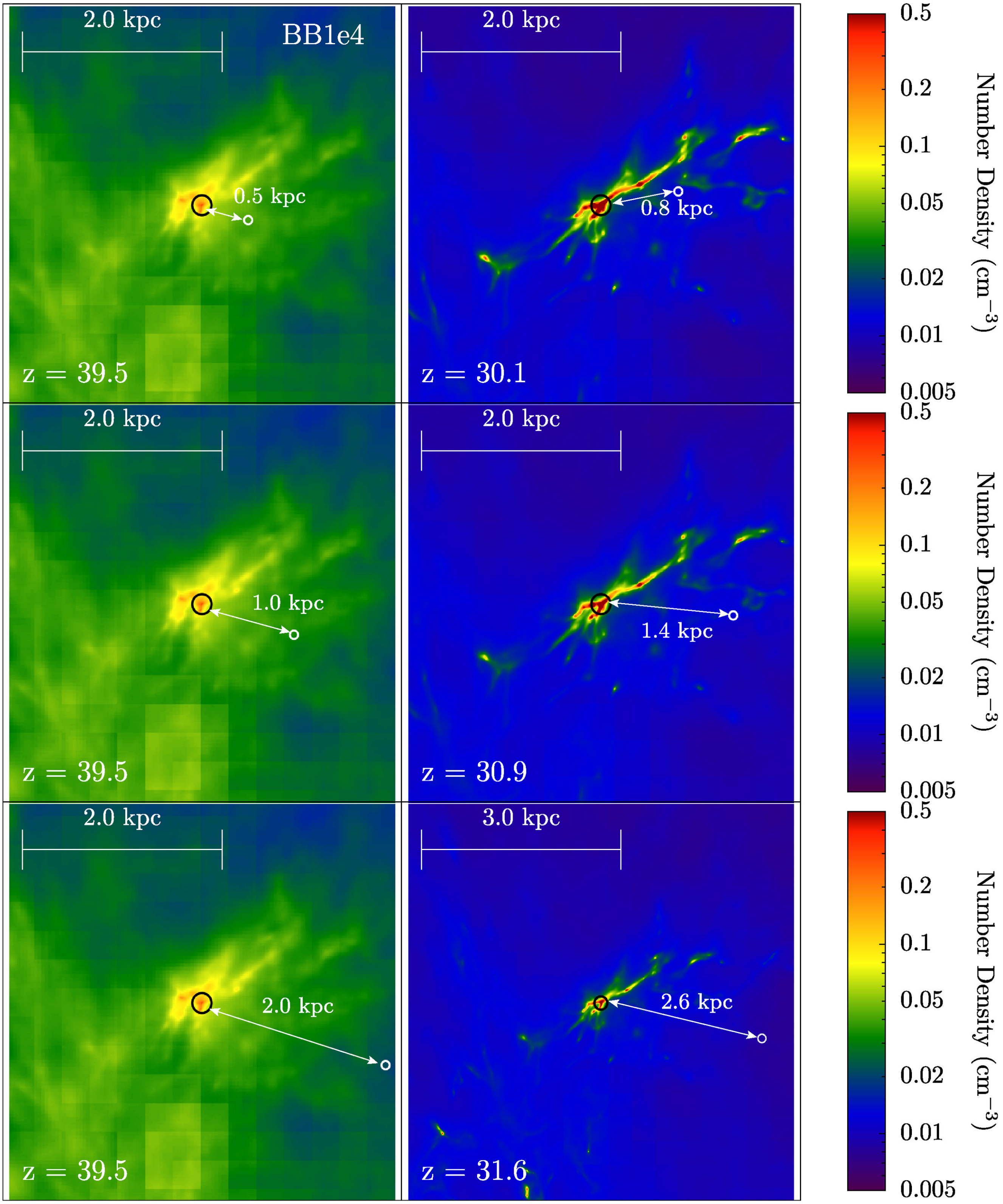

Figure 3. The figure contains projections for the three models run with a blackbody spectrum with $T = 10^4$ K (BB1e4). In the top row, we show the model where the source is set at an initial distance of 0.5 kpc from the target halo, in the middle row, the source is placed at a distance of 1.0 kpc, while in the bottom row, the source is placed at a distance of 2.0 kpc. In the left-hand column, we show the setup a short time after the source is switched on, at a redshift of 39.5. In the right-hand column, we show the final output of the simulation. The source is marked with a white circle. The point of maximum density is identified with a black circle. The larger distances between the source and the point of maximum density shown in the right-hand column is due to the expansion of the universe over the given redshift interval.

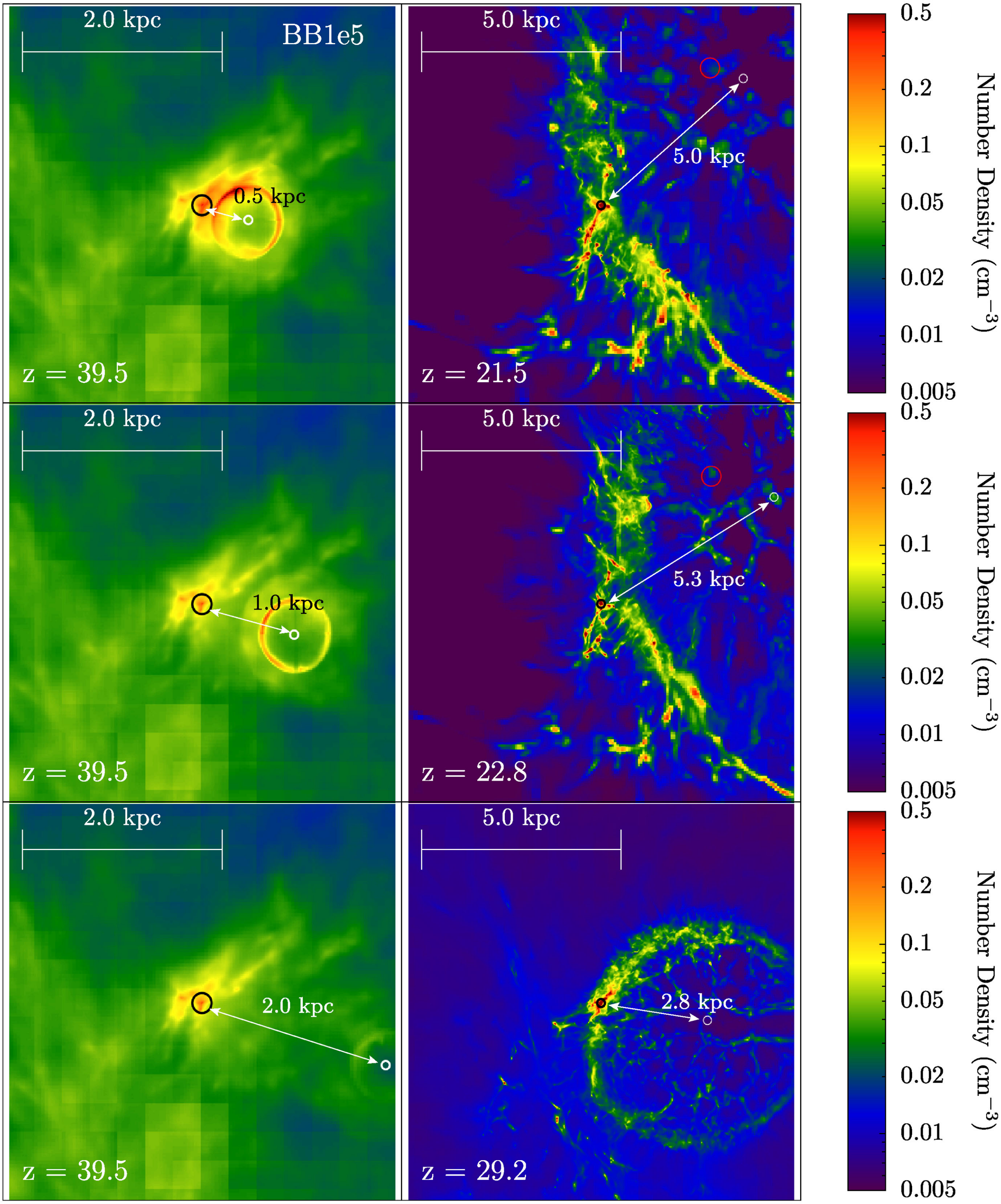

Figure 4. The figure contains projections for the three models run with a blackbody spectrum with $T = 10^5$ K (BB1e5). In the top row, we show the model where the source is set at an initial distance of 0.5 kpc from the target halo, in the middle row, the source is placed at a distance of 1.0 kpc, while in the bottom row, the source is placed at a distance of 2.0 kpc. In the left-hand column, we show the setup a short time after the source is switched on, at a redshift of 39.5. In the right-hand column, we show the final output of the simulation. The source is marked with a white circle. The point of maximum density is identified with a black circle. The larger distances between the source and the point of maximum density shown in the right-hand column is due to the expansion of the universe over the given redshift interval. The red circle in the top-right panel and the middle-right panel indicates the approximate location of the original target halo (which is completely disrupted).

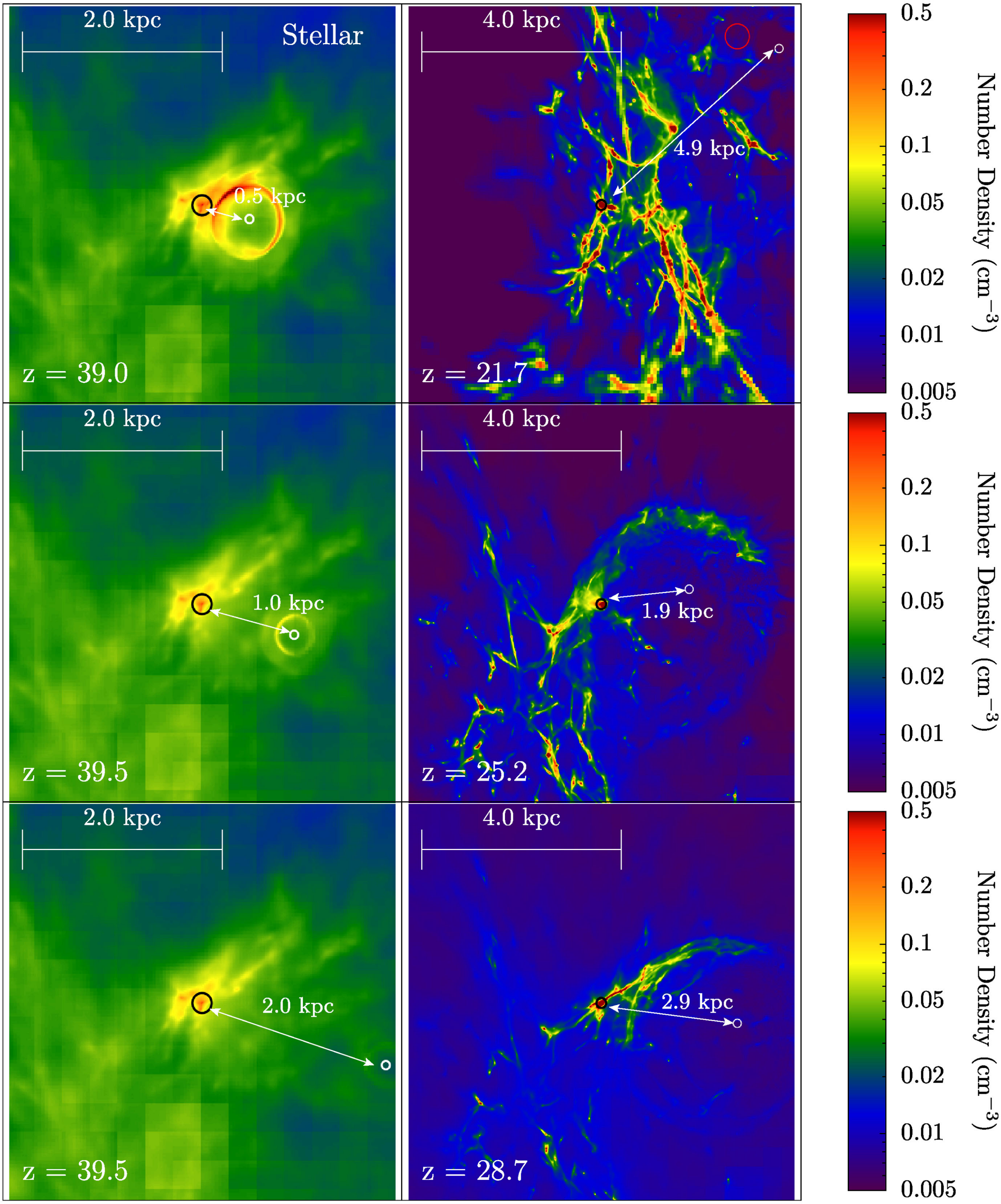

Figure 5. The figure contains projections for the three models run with a realistic stellar SED. In the top row, we show the model where the source is set at an initial distance of 0.5 kpc from the target halo, in the middle row, the source is placed at a distance of 1.0 kpc, while in the bottom row, the source is placed at a distance of 2.0 kpc. In the left-hand column, we show the setup a short time after the source is switched on, at a redshift of 39.5. In the right-hand column, we show the final output of the simulation. The source is marked with a white circle. The point of maximum density is identified with a black circle. The larger distances between the source and the point of maximum density shown in the right-hand column is due to the expansion of the universe over the given redshift interval. The red circle in the top-right panel indicates the approximate location of the original target halo (which is completely disrupted).

3.1.2 Blackbody with $T = 10^5$ K (BB1e5)

In Fig. 4, the models for a source with a blackbody spectrum of $T = 10^5$ K (BB1e5) is plotted. In this case, the target halo and the collapse halo do not match when the source is placed at a distance of 1 or 0.5 kpc. Cosmic expansion will account for an approximate doubling of the physical distance between the source and the target halo from $z = 40$–20, while in the 0.5 and 1.0 kpc cases, the distance between the source and the target halo is significantly greater by a factor of 2. We have marked the approximate location of the target halo's position in these projections using a red circle. The radiation from the source in this case has completely disrupted the target halo. The ionizing radiation with energy greater than 13.6 eV has prevented the halo from cooling and has also heated the gas further reducing its ability to cool. The result is that a halo at larger distances from the source has collapsed. When the source is placed further from the target halo – at a distance of 2 kpc – the target halo and the collapse halo remain the same and target halo collapses at a redshift of $z = 29.2$. In the 05-T5 and 1-T5 cases, the collapse occurs at the edge of the H II region. Within this shell, collapse is prevented by the ionizing radiation field which prevents efficient cooling of the gas. On the H II shell, the gas is able to cool and condense and in both cases, a collapse occurs. The 2-T5 model is not hampered in the same way. In this case, the H II region again forms and this is seen quite clearly in the bottom row of Fig. 4. In this case, the H II region is unable to envelop the target halo before it collapses. From the projection, it can be clearly seen that the target halo is collapsing just outside the H II region and so it is able to escape the damaging effects of the ionizing radiation on its ability to cool.

3.1.3 Stellar spectrum

In Fig. 5, the models for the source with a stellar like spectrum are shown. Again the column on the left shows the source and target halo shortly after the source is turned on. The column on the right shows the collapsed halo at the final output time. The outline of the H II region is clearly visible in the middle and bottom rows of the plots. In the top row, the initial distance to the target halo is set to be 0.5 kpc. The ionizing radiation overwhelms the target halo in this instance and that halo is then not the first halo to collapse. Rather in this case, a halo at 5.0 kpc from the source collapses first – outside the sphere of influence of the ionizing radiation. In this case, the halo again collapses just outside the H II region where dense gas is able to cool effectively. Again we have marked the position of the original target halo with a red circle. In the middle row, the target halo does undergo collapse. The distance to the target halo at the time of collapse is 1.9 kpc (as expected) and the halo lies close to the edge of the H II region. In the bottom row, the target halo is again the collapse halo with a distance from the source of 2.9 kpc. The halo lies just outside the H II region in this case and so again is able to collapse. We will now examine the collapse of each halo more quantitatively.

3.2 Ray profiling

3.2.1 Blackbody with $T = 10^4$ K

In Figs 6–8, we have plotted ray profiles from the source to the collapsing halo. The shown profiles are averaged over 1000 sightlines. The lines all start from the source and travel to an area surrounding the collapsing halo. The first sightline always connects the source and the point of maximum density. Each subsequent sightline is given a small (randomly generated) angular offset so that it traverses a slightly different path to the central region, thus defining a circular region around the central region from which the sightlines are extracted. In Fig. 6, we show the ray profiles for all of the models for the blackbody source with a temperature of $T = 10^4$ K. For each source with a different initial distance, we show the ray profile at $z = 36.0$ (before any collapse) and at the collapse redshift.

Given that the flux received at the target halo is significantly different at the time of collapse (see bottom-right panel of Fig. 6), the overall characteristics of the haloes are still quite similar. In all cases, the temperature at the centre of the halo converges to approximately $T = 700$ K and the H_2 fraction is also approximately the same in each case. Some differences emerge at a distance of greater than approximately 1 pc. Within 1 pc, self-shielding of H_2 takes over meaning that within this radius, the dissociating radiation has little effect and hence we see similar characteristics across all three models within this radius. At a radius greater than 1 pc, the effects of the dissociating radius are more obvious and we see that the model with an initial separation of 2 kpc has a systematically reduced temperature (red line) at almost all scales. This is due to the enhanced H_2 fraction compared to the other models where the source is placed closer to the target halo. The dissociating H_2 radiation is unable to destroy the H_2 as efficiently and the cooling due to H_2 is more effective. For cases where the source has an initial separation of 0.5 kpc or 1 kpc, the quantitative and qualitative differences are rather small. The flux reaching the central object in both of these cases is approximately 2.0 J_{21} for an initial separation of 0.5 kpc and 1 J_{21} for an initial separation of 1.0 kpc.

3.2.2 Blackbody with $T = 10^5$ K

In Fig. 7, we show the ray profiles for the spectrum with a blackbody temperature of $T = 10^5$ K. The radiation peak in this case is closer to the LW band (see Fig. 1) and so the effect of the H_2 dissociation is more clearly evident closer to the source – see top-left panel of Fig. 7 and compare to the top-left panel of Fig. 6. The temperature profiles are also quite different compared to the blackbody spectrum with $T = 10^4$ K. This is because the spectrum with a blackbody of $T = 10^5$ K both heats the gas and also disrupts its ability to cool by ionizing hydrogen. As a result, we do not observe the characteristic shock heating at the virial radius seen in the profile plots of Fig. 6 at a radius of approximately 10–100 pc. Instead, the gas begins to cool due to Lyman α and recombination cooling as we move away from the source. In the centre of the halo where the H_2 fractions are able to self-shield and H_2 cooling can continue unabated the temperature drops to $T \sim 1000$ K. These temperatures are similar to what was observed in Fig. 6 and reflects the fact that H_2 shielding is able to block the effects of LW radiation in both cases resulting in similar levels of H_2 in both cases. What is also evident from Fig. 7 is that the destruction of H_2 is not a smoothly varying function of distance as was seen in Fig. 6. In the case of the $T = 10^5$ K spectrum, we also now have hydrogen ionizing radiation. This radiation produces free electrons from the ionization process. These electrons are then free to combine with the remaining neutral hydrogen or ionized hydrogen which is recombining. The increase in the H^- fraction can increase the H_2 fraction at small distances from the source. However, the hydrogen ionizing radiation has a shorter mean free path than the LW radiation and so we see a dip again in the H_2 fraction (top-left panel) before it quickly rises again as the effects of an increasing H_2 column density become more apparent.

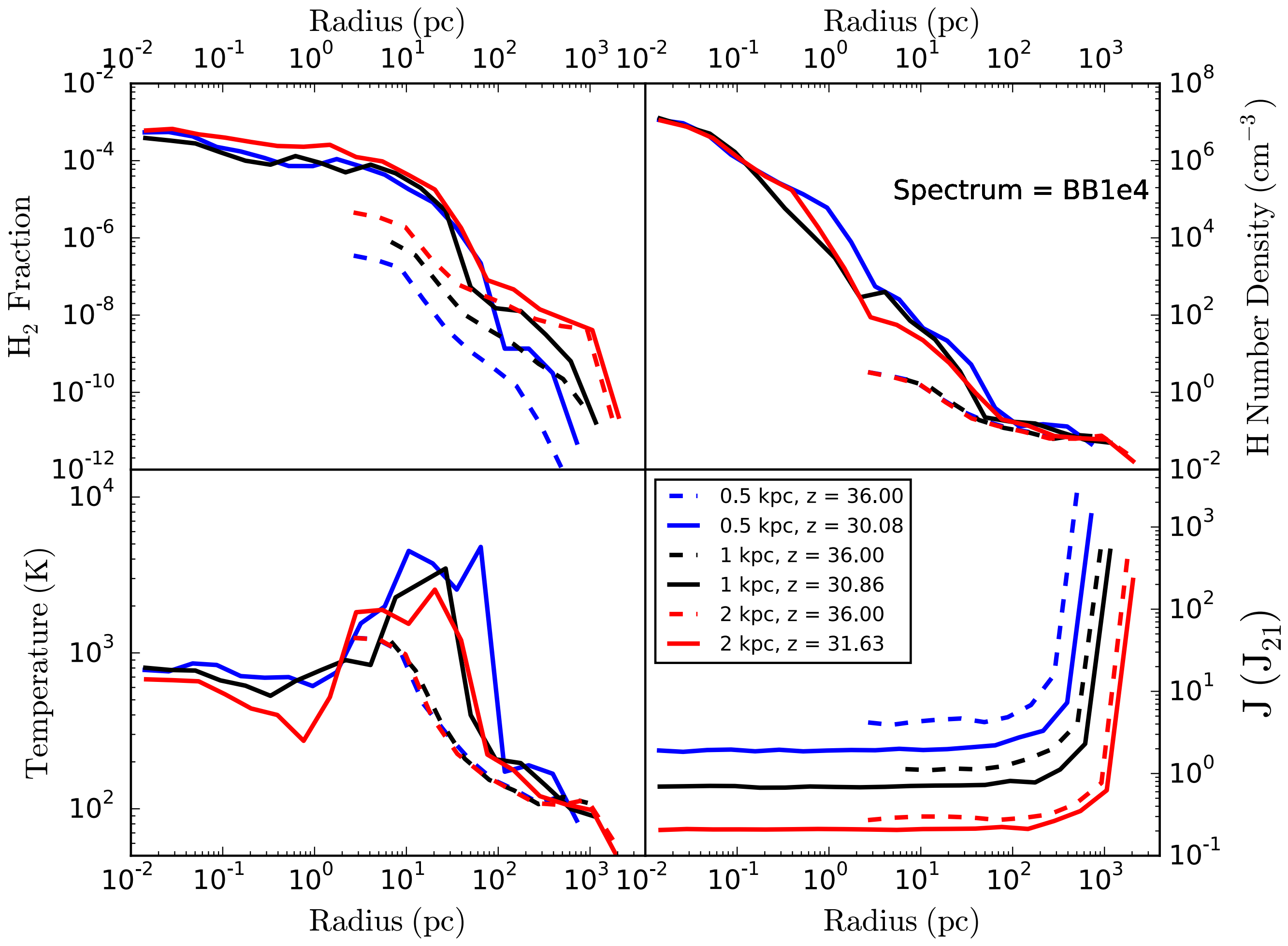

Figure 6. BB1e4: ray profiles for when the halo is exposed to a radiation source with a 10 000 K blackbody spectrum. In each panel, the quantity displayed is a function of radius along 1000 sightlines from the radiation source to the central density at each redshift. The top-left panel shows the H_2 fraction, the top-right panel shows the hydrogen number density, the bottom-right panel shows the value of the intensity, J, in the usual units of 10^{-21} erg cm^{-2} s^{-1} Hz^{-1} sr^{-1}, the bottom-left panel shows the temperature.

3.2.3 Stellar spectrum

In Fig. 8, we show the result from the ray profiles due to the source with a stellar-like SED. This SED resembles a combination of the $T = 10^4$ K blackbody spectrum and the $T = 10^5$ K blackbody spectrum. The temperature profiles are quite similar to those from the $T = 10^5$ K blackbody spectrum. However, in the case of both the source at an initial distance of 0.5 and 2 kpc, there is a clear cooling of the gas outside of the virial radius of the collapsing halo (red and green solid lines). The reason for this is that there is less radiation with energies greater than 13.6 eV compared to the blackbody spectrum with $T = 10^5$ K. In the case of the 0.5 kpc source, this is because the collapse halo is located quite far from the source – at a final separation of ∼5.0 kpc, while in the case of the source with an initial separation of 2.0 kpc, the final separation is 2.9 kpc. In both cases, the H II region surrounding the source does not reach the virial radius of the collapsing halo. As a result, there is a clear shock at the virial radius for these two cases and the gas heats up. For the case of the source with an initial separation of 1 kpc, the effects of photoheating and ionization are felt up and inside the virial radius of the collapsing halo (because the final separation is 1.9 kpc – just inside the H II region). As with the $T = 10^5$ K spectrum, the H_2 fraction shows a very strong drop close to the source before rising quickly due to the presence of free electrons which facilitates the production of H_2. As the free electron fraction drops, we again see a decrease in the H_2 fraction as the catalyst (free electrons) is not available to facilitate the production of H_2. This effect is clearly seen in both the 05-SSED and 2-SSED models. The H_2 fraction then increases slowly as the flux reduces before we finally enter the self-shielded region within approximately 0.1–1.0 pc of the central object. The values of the flux at the centre of the collapsing halo vary between 1 and 10 J_{21} for this realistic source. The blue solid line with a flux of less than 1 J_{21} in Fig. 8 results because the collapsing halo in this case is not the target halo. The collapsing halo in this case (see Fig. 5) collapses at a distance of ∼5.0 kpc from the source and hence the flux at the point is relatively low.

3.3 Increasing the source distance

In Fig. 9, we show the result of ray profiling for the stellar spectrum case when the source is moved to a distance of 4, 8 and 12 kpc from the target halo, respectively. The 4-SSED model is very similar at every scale to the 2-SSED model. However, significant differences emerge once the source is moved to 8 and 12 kpc. In these cases, the temperature is systematically lower at almost all scales of interest.

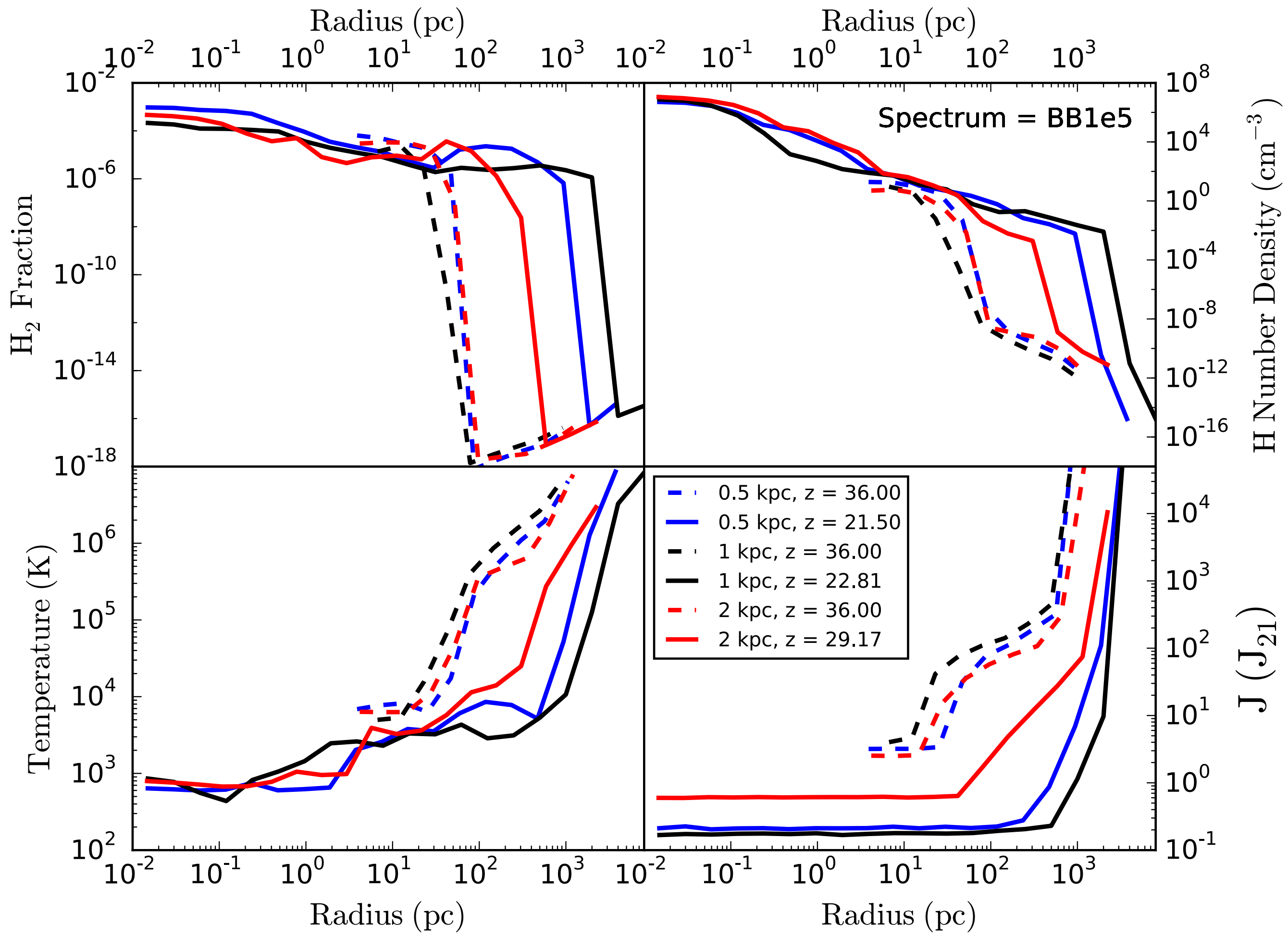

Figure 7. BB1e5: ray profiles for when the target halo is exposed to a radiation source with a 100 000 K blackbody spectrum. In each panel, the quantity displayed is a function of radius along 1000 sightlines from the radiation source to the central density at each redshift. The top-left panel shows the H_2 fraction, the top-right panel shows the hydrogen number density, the bottom-right panel shows the value of the intensity, J, in the usual units of 10^{-21} erg cm^{-2} s^{-1} Hz^{-1} sr^{-1}, the bottom-left panel shows the temperature.

The reason for this is clear from the H_2 fraction plot in the top-left panel. Between approximately 1 pc and 50 pc from the central region, the H_2 fraction in each case differs by up to an order of magnitude. The increased level of H_2 in the 12-SSED results in a lower temperature on average over that range. The characteristics of model 12-SSED are becoming very similar to those of the no radiation case as shown in Table 2 reflecting the fact that at these distances, the radiative flux has a rather small effect on the dynamics of the halo.

3.4 Mass inflow rates

In Fig. 10, we have plotted both the mass inflow rates and the enclosed mass at the final output time for models with a stellar spectrum and a range of initial distances. The mass inflow rates are calculated using the radial velocity as follows

$$\dot{M}(t) = 4\pi R^2 \rho(R) V(R), \tag{14}$$

where $\dot{M}(t)$ is the mass inflow rate, R is the radius, ρ is the density and $V(R)$ is the radial velocity at R. For all values, we choose spherically averaged quantities centred on the point of maximum density. While this is clearly an approximation to the true mass inflow rate, which will likely be episodic and possibly anisotropic, it does provide us with an insight into the gas dynamics as a function of radius. The anisotropic nature of our radiation source is only significant outside of approximately 100 pc from the centre and hence we consider here spherical profiles within the central 100 pc. In the left-hand panel of Fig. 10, we have plotted a radial profile of the enclosed gas mass for models with initial separations of 0.5 kpc up to 12 kpc, we have also plotted the values in the case where no radiation field is used (Ctrl model). The key point is that as the radiation flux increases, we see a proportional increase in the enclosed gas mass at a given radius. If we consider the core radius to be 1 pc, we see that the enclosed mass at this point is between approximately 10 000 $M_{\odot}$for the 1-SSED case down to approximately 1000 $M_{\odot}$for the Ctrl case.

Of equal importance is the mass inflow rate on to the central object which is a critical component in determining the final outcome of the central object (see Section 4). In the right-hand panel, we have plotted the mass inflow rate at the final output time for the same range of models. The inflow rates vary somewhat over time but generally increase as the collapse proceeds. The 1-SSED, 2-SSED and 4-SSED models show strong inflow rates between a few tenths of a parsec out to several tens of parsecs with an average mass inflow

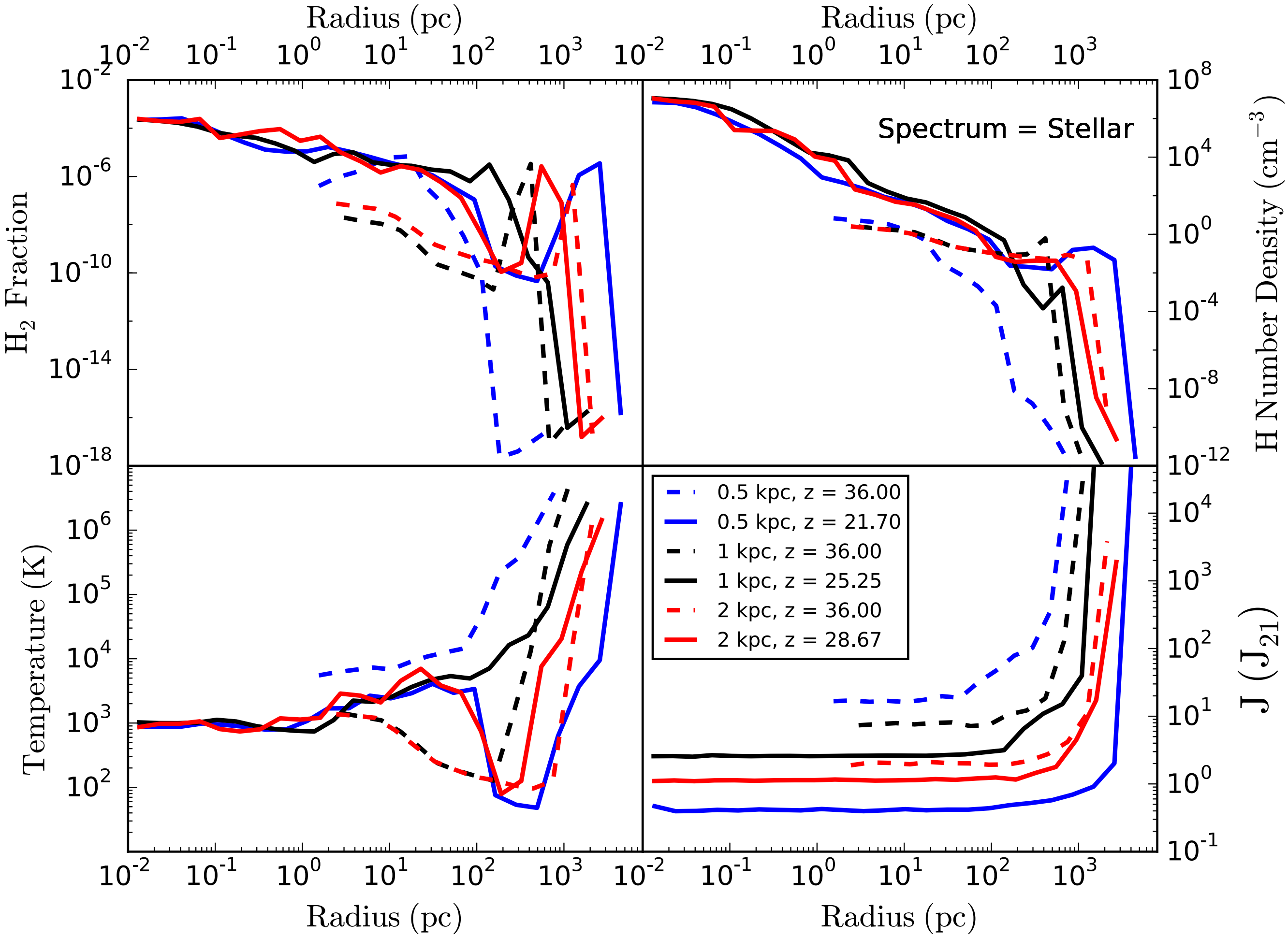

Figure 8. Stellar SED: ray profiles for when the target halo is exposed to a radiation source based on a realistic stellar SED. In each panel, the quantity displayed is a function of radius long 1000 sightlines from the radiation source to the central density at each redshift. The top-left panel shows the H_2 fraction, the top-right panel shows the hydrogen number density, the bottom-right panel shows the value of the intensity, *J*, in the usual units of 10^{-21} erg cm^{-2} s^{-1} Hz^{-1} sr^{-1}, the bottom-left panel shows the temperature.

rate of $\sim$0.1 M$_\odot$ yr^{-1} over that range. The values in this case are consistent with those of Hosokawa et al. (2013) and Schleicher et al. (2013) who advocate values of $\gtrsim$0.1 M$_\odot$ yr^{-1} are required for the formation of supermassive stars or quasi-stars.

As the flux drops (or equivalently as the distance to the source increases), the mass inflow rates drop systematically. It should also be noted that the value of the mass inflow rates for model 2-SSED are strongly peaked at a radius of $\sim$2 pc. This is due to the dynamics of the collapse of this particular model. A full analysis of the accretion rate on to a central object, the subsequent evolution and the associated feedback effects is beyond the scope of this study.

4 DISCUSSION

This study has focused on examining the effect of stellar radiation from a realistic source halo on the collapse of a neighbouring or satellite halo. As a consequence of this study, several points are worth noting.

(i) Our most promising candidate for forming a DCBH is the 1-SSED simulation. The halo collapses at a redshift of $z = 25.25$ with a virial temperature of $T_{\rm vir} \sim 9500$ K. The mass inflow rate on to the halo is extremely high at the time of collapse with a mass inflow rate of $\gtrsim$ 0.1 M$_\odot$ yr^{-1}. The gas mass within the central core ($\sim$1 pc) is $\sim$10 000 M$_\odot$ and the gas is hot with temperatures up to 10 000 K at the virial radius ($R_{\rm vir} \sim 300$ pc). At the time of collapse, the distance between the central object and the radiation source is $\sim$1.9 kpc.

(ii) Using the stellar spectrum as the most realistic spectrum models 2-SSED, 4-SSED, 8-SSED are also candidates. However, in all of these cases, the temperature and enclosed mass values drop as the distance to the radiation source increases. Further investigation of the collapse physics and the impact of the surrounding mass envelope out to distances of a few hundred parsecs will be required to clearly distinguish those haloes which can and cannot form DCBH seeds.

(iii) The ionizing region can completely disrupt the collapse if the radiating halo is too close to the target halo. In three cases, 05-T5, 1-T5 and 05-SSED, we saw that the target halo is unable to collapse and a different minihalo approximately 5.0 kpc from the radiating source ultimately collapses first. The fact that the target halo is enveloped within the H II region of the source halo means that its collapse at a later stage is unlikely (as long as the H II region remains). Furthermore, due to the close proximity of the target

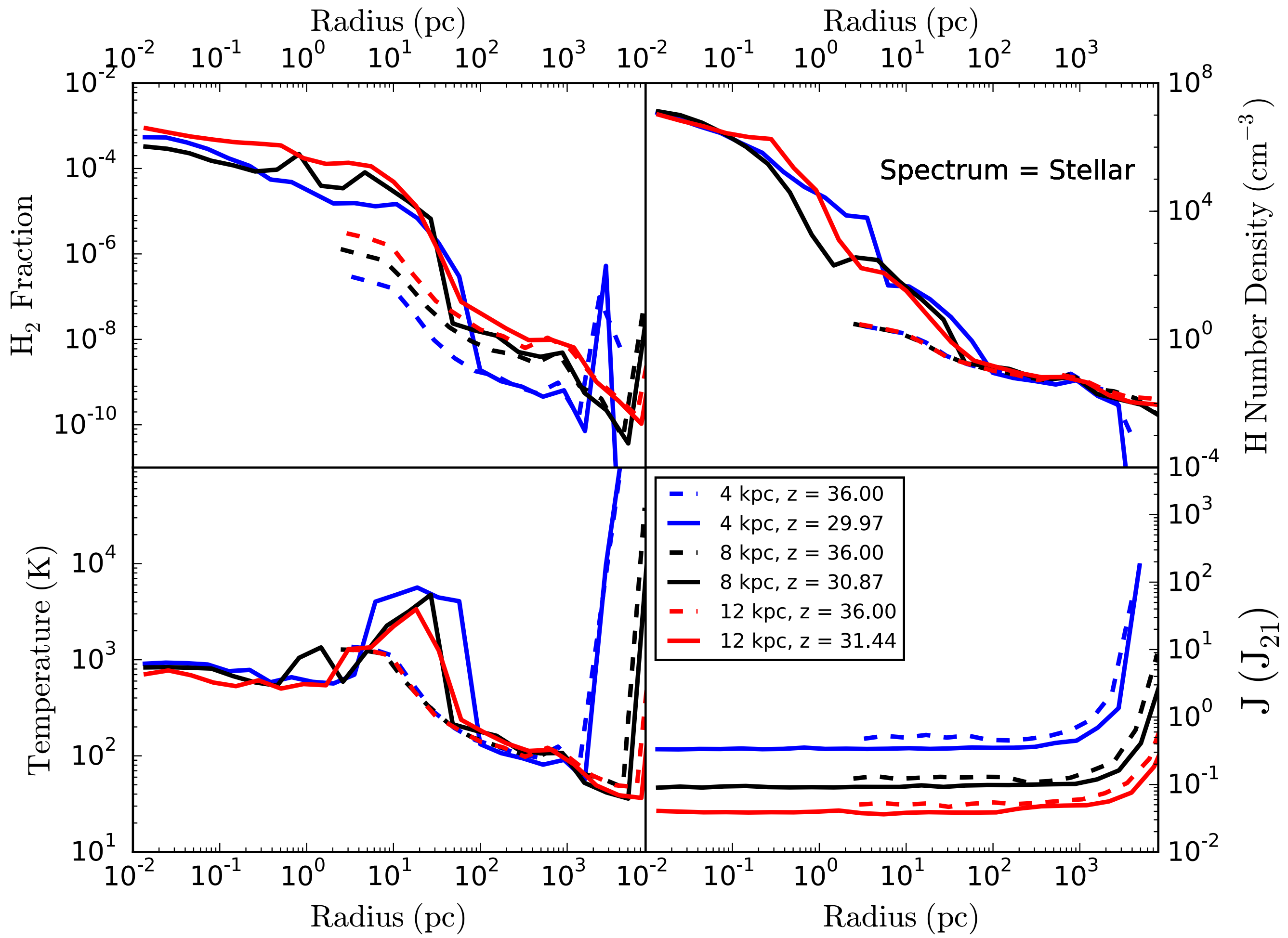

Figure 9. Stellar SED at increased distances: ray profiles showing the effect of radiation at greater distances. As we increase the distance, the temperature within the virial radius (∼ 10–100 pc) systematically decreases for the models as the initial separation is varied from 4 to 12 kpc. As we move to 12 kpc, the temperature variation is clearly smaller and saturation is setting in. In all three cases, the primary coolant is H_2 – the H_2 rises above a mass fraction 10^{-6} at approximately 75 pc giving virial temperatures of $\lesssim$3000 K is each case.

halo to the collapse, the target halo is likely to become polluted by metals due to winds from the radiating source particularly for the cases where the halo is placed at the shorter distances of 0.5 kpc.

(iv) For the cases where the target halo is completely disrupted a halo on the edge of the H II region collapses which is different from the original target halo. The virial temperature in each case is greater than 8000 K and therefore atomic cooling is operational. Taking the 05-SSED as the best example, the characteristics of the 05-SSED case are somewhat similar to the 1-SSED case. The major difference is that the flux is lower by a factor of 10 (because the collapsed halo is now ∼5.0 kpc from the source) and the temperature of the gas at a radius of approximately 200 pc is also significantly higher. This impacts on the effects of the LW radiation at this scale, the H_2 fraction between ∼10 and 500 pc is in fact higher in the 1-SSED case contrary to what might be naively expected. This is a direct result of the higher gas temperature of the gas at this scale.

(v) The mass inflow rates found in our simulations have peaks that are greater than 0.1 $M_\odot$ yr^{-1}. In particular, models 1-SSED, 2-SSED and 4-SSED have sustained average inflow rates of ∼0.1 $M_\odot$ yr^{-1} over a decade or more in radius. These values for the mass inflow rate compare well to what has been suggested is required for supermassive star or quasi-star formation by Hosokawa et al. (2013) and Schleicher et al. (2013). However, we do not attempt, in these simulations, to follow the collapse to very small scales and lack the necessary resolution and detailed physics to make firm predictions on the characteristics of the final object. Recent work by Hosokawa et al. (2015) also indicates that short accretion bursts temporarily exceeding 0.01 $M_\odot$ yr^{-1} may be all that is required to induce massive primordial star formation which could in turn result in DCBH seeds. It would appear from our simulations that achieving this criteria should at least be feasible.

(vi) The flux at this redshift is limited by the available growth time. Our stellar flux was limited to 1.2×10^{52} photons per second based on a stellar mass of 10^5 $M_\odot$ at $z = 20$. Achieving significantly higher fluxes at this redshift is unlikely and the values of J found in our simulations represent likely values at this epoch ($J \sim 10$ J_{21} for the 1-SSED model). Moreover, in our simulations, the source radiates at this flux starting from $z = 40$ meaning that this is a rather optimistic and somewhat idealized case. More realistic cases (even rare ones) would start off with much lower fluxes. Our values are not high enough to halt H_2 cooling completely especially towards the centre of the halo and as a result, the temperature of the gas found in the centres of haloes are well below those found in atomic cooling haloes by approximately an order of magnitude. Hence,

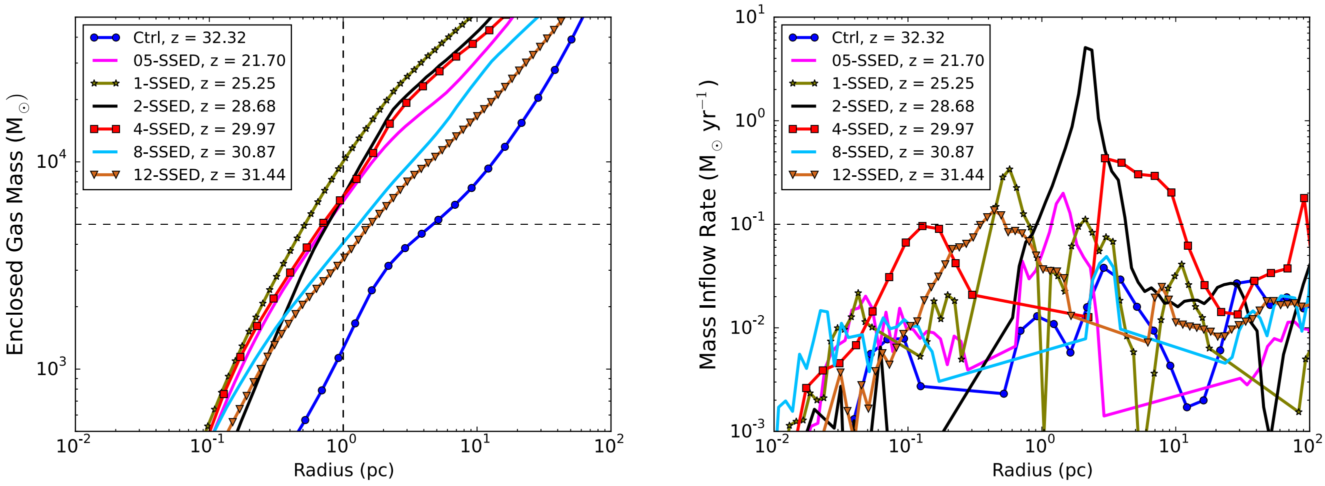

Figure 10. In the left-hand panel, we have plotted the enclosed mass for all the simulations run with a stellar SED. We have also included the control run which features no radiation source for comparison. The key point is that the runs with a higher radiation source have more gas at each radii. For example, at a radius of 1 pc, there is approximately 10 times more mass at that radius in the 1-SSED compared to the control case. The dashed lines are at a radius of 1 pc and an enclosed mass of 5000 M$_\odot$and are merely to guide the eye. In the right-hand pane,l we have plotted the associated mass inflow rates as a function of radius. Only the control model (Ctrl) and the 8-SSED model have rates which do not exceed 0.1 M$_\odot$ yr^{-1} at some radius. The 2-SSED model exceeds 1 M$_\odot$ yr^{-1} at a radius of ∼2 pc and is likely due to the state of the gas at this output. Overall the rates are as expected with the highest inflow rates occurring for the haloes exposed to the most intense radiation field. We also add a note of caution when comparing to the 05-SSED run that it is not the same halo as in each of the other cases. In both panels, we have 'zoomed in' on the available ranges for illustration.

the formation of a truly atomic core, if required for DCBH seed formation (see Latif & Volonteri 2015), may need to wait until lower redshifts where a combination of a background and nearby source can generate a high enough *J*.

(vii) The recent identification of a very bright Lyman α emitter discovered at $z \sim 6.6$ (Matthee et al. 2015; Sobral et al. 2015) has been followed up by some theoretical studies proposing that the Lyman α source may be a DCBH (Agarwal et al. 2015; Hartwig et al. 2015; Pallottini et al. 2015). In particular, Agarwal et al. (2015) find that, in modelling CR7, DCBH formation occurs in the range $19 < z < 23$. In our simulations, by turning on our initial (atomic halo) source at $z = 40$, we find that we can form near-atomic cooling haloes between $z \sim 20$ and 26. These haloes have virial temperatures between 7000 and 10 000 K. As discussed above, model 1-SSED would provide a good fit to the results of Agarwal et al. (2015). However, the core is primarily cooled by H_2 and the fate of the central object is unclear. Further study of the detailed physics of the collapse in this scenario is the next logical step.

(viii) To simulate a nearby atomic cooling halo hosting a galaxy, we use a radiation particle to model the emission. We do this so as to increase the flexibility of our parameter study and this allows us to easily alter the distance from the radiating galaxy to the target halo. It should be noted, however, that we miss some important considerations in this case. In particular, these systems, given their close proximity, are likely bound systems and this is not taken into account in our model. Nor is the fact that as the evolution proceeds, these systems may decrease in separation and may in fact merge. This scenario will be be investigated in an upcoming study (Regan et al. 2016).

5 CONCLUSIONS

Using a multifrequency ray-tracing scheme, we have investigated the impact of three different spectral shapes on a collapsing halo. We have used a blackbody spectrum with $T = 10^4$ K, a blackbody spectrum with $T = 10^5$ K and a spectrum with a spectral shape consistent with that produced by a galaxy at $z \sim 20$. In each case, the photon emission rate is unchanged and has been set to 1×10^{52} photons s^{-1} consistent with simulations of the first galaxies (Chen et al. 2014). To model the emitting galaxy which is supposed to reside close to the collapsing halo, we have developed a radiation particle which we place at fixed initial distances from the halo. We vary these initial distances between 0.5 and 12 kpc from the halo to investigate the impact of the radiation on the collapsing halo. The radiation covers the range 0.1–60 eV.

Using the stellar spectrum as our fiducial result, we find that placing the source too close to the collapsing halo (distance less than 1.0 kpc) results in the total disruption of the collapsing halo due to photoionization of hydrogen. As the source is moved further from the halo, we find that at distances greater than 4 kpc, the intensity of the radiation impacting the halo is at or below what would be expected from the background at high redshift. The resulting virial temperatures of the collapsed halo are well below that where atomic processes dominate and as a result, the halo is unlikely to be a candidate for forming direct collapse seeds.

At initial separations of 1 kpc (and 2 kpc) we are able to form haloes with virial temperatures greater than 6000 (4000) K. Crucially, in the case of the source at a separation of 1 kpc (model 1-SSED), the object that forms at the centre of this halo is surrounded by a large envelope of hot gas with an enclosed mass nearly 10 times greater than what is observed in the haloes subjected to weaker radiation fields. Furthermore, the mass inflow rates observed for this halo have average values greater than ∼0.1 M$_\odot$ yr^{-1} out to several tens of parsecs. These environmental conditions favour the formation of extremely massive primordial stars (Schleicher et al. 2013; Hosokawa et al. 2013, 2015), in neighbouring satellite haloes, and could potentially be the ideal environment in which to form massive black hole seeds. Further investigation of the detailed physics of the collapse, given these environmental conditions, is now required to determine the exact nature of what object(s) form and whether they can then collapse to form a massive black hole seed.

ACKNOWLEDGEMENTS

JAR and PHJ acknowledge the support of the Magnus Ehrnrooth Foundation, the Research Funds of the University of Helsinki and the Academy of Finland grant 1274931. This work was also supported by the Science and Technology Facilities Council [ST/F001166/1]. JHW acknowledges support by NSF and NASA grants AST-1333360 and HST-AR-13895.001. The numerical simulations were performed on facilities hosted by the CSC -IT Center for Science in Espoo, Finland, which are financed by the Finnish ministry of education. Computations described in this work were performed using the publicly available ENZO code (http://enzo-project.org), which is the product of a collaborative effort of many independent scientists from numerous institutions around the world. Their commitment to open science has helped make this work possible. The freely available astrophysical analysis code YT (Turk et al. 2011) was used to construct numerous plots within this paper. The authors would like to express their gratitude to Matt Turk et al. for an excellent software package. All modified source code used in this work is freely available from JAR's bitbucket account and is in the process of being pushed to the Grackle and Enzo mainlines. Email JAR for more information on acquiring the updated source code if required. Finally, the authors would like to thanks an anonymous referee for a detailed and helpful report.

REFERENCES

Abel T., Anninos P., Zhang Y., Norman M. L., 1997, New Astron., 2, 181
Agarwal B., Khochfar S., 2015, MNRAS, 446, 160
Agarwal B., Davis A. J., Khochfar S., Natarajan P., Dunlop J. S., 2013, MNRAS, 432, 3438
Agarwal B., Dalla Vecchia C., Johnson J. L., Khochfar S., Paardekooper J. P., 2014, MNRAS, 443, 648
Agarwal B., Johnson J. L., Zackrisson E., Labbe I., van den Bosch F. C., Natarajan P., Khochfar S., 2015, preprint (arXiv:1510.01733)
Agarwal B., Smith B., Glover S., Natarajan P., Khochfar S., 2016, preprint (arXiv:1504.04042)
Alvarez M. A., Wise J. H., Abel T., 2009, ApJ, 701, L133
Black J. H., 1981, MNRAS, 197, 553
Bromm V., 2013, Rep. Prog. Phys., 76, 112901
Bromm V., Loeb A., 2003, ApJ, 596, 34
Bruzual G., Charlot S., 2003, MNRAS, 344, 1000
Bryan G. L., Norman M. L., O'Shea B. W., Abel T., Wise J. H., Turk M. J., The Enzo Collaboration, 2014, ApJS, 211, 19
Chen P., Wise J. H., Norman M. L., Xu H., O'Shea B. W., 2014, ApJ, 795, 144
Clark P. C., Glover S. C. O., Klessen R. S., Bromm V., 2011, ApJ, 727, 110
Coppola C. M., Longo S., Capitelli M., Palla F., Galli D., 2011, ApJS, 193, 7
Coppola C. M., D'Introno R., Galli D., Tennyson J., Longo S., 2012, ApJS, 199, 16
Croft H., Dickinson A. S., Gadea F. X., 1999, MNRAS, 304, 327
Dijkstra M., Haiman Z., Mesinger A., Wyithe J. S. B., 2008, MNRAS, 391, 1961
Dijkstra M., Ferrara A., Mesinger A., 2014, MNRAS, 442, 2036
Dove J. E., Rusk A. C. M., Cribb P. H., Martin P. G., 1987, ApJ, 318, 379
Fan X. et al., 2006, AJ, 132, 117
Ferland G. J., Peterson B. M., Horne K., Welsh W. F., Nahar S. N., 1992, ApJ, 387, 95
Fernandez R., Bryan G. L., Haiman Z., Li M., 2014, MNRAS, 439, 3798
Field G. B., Somerville W. B., Dressler K., 1966, ARA&A, 4, 207
Forrey R. C., 2013, ApJ, 773, L25
Glover S. C. O., 2015a, MNRAS, 451, 2082
Glover S. C. O., 2015b, MNRAS, 453, 2901
Glover S. C. O., Abel T., 2008, MNRAS, 388, 1627
Glover S. C. O., Jappsen A. K., 2007, ApJ, 666, 1
Glover S. C. O., Savin D. W., 2009, MNRAS, 393, 911
Górski K. M., Hivon E., Banday A. J., Wandelt B. D., Hansen F. K., Reinecke M., Bartelmann M., 2005, ApJ, 622, 759
Greif T. H., Springel V., White S. D. M., Glover S. C. O., Clark P. C., Smith R. J., Klessen R. S., Bromm V., 2011, ApJ, 737, 75
Guberman S. L., 1994, Phys. Rev. A, 49, 4277
Hahn O., Abel T., 2011, MNRAS, 415, 2101
Haiman Z., Abel T., Rees M. J., 2000, ApJ, 534, 11
Hartwig T. et al., 2015, preprint (arXiv:1512.01111)
Hirano S., Hosokawa T., Yoshida N., Umeda H., Omukai K., Chiaki G., Yorke H. W., 2014, ApJ, 781, 60
Hosokawa T., Omukai K., Yoshida N., Yorke H. W., 2011, Science, 334, 1250
Hosokawa T., Yorke H. W., Inayoshi K., Omukai K., Yoshida N., 2013, ApJ, 778, 178
Hosokawa T., Hirano S., Kuiper R., Yorke H. W., Omukai K., Yoshida N., 2015, preprint (arXiv:1510.01407)
Hummer D. G., Storey P. J., 1998, MNRAS, 297, 1073
Inayoshi K., Omukai K., 2011, MNRAS, 416, 2748
Inayoshi K., Omukai K., 2012, MNRAS, 422, 2539
Inayoshi K., Tanaka T. L., 2015, MNRAS, 450, 4350
Inayoshi K., Visbal E., Kashiyama K., 2015, MNRAS, 453, 1692
Janev R. K., Langer W. D., Evans K., 1987, Elementary Processes in Hydrogen-Helium Plasmas – Cross-sections and Reaction Rate Coefficients. Springer, Berlin
Johnson J. L., Bromm V., 2007, MNRAS, 374, 1557
Johnson J. L., Greif T. H., Bromm V., 2008, MNRAS, 388, 26
Juřek M., Špirko V., Kraemer W. P., 1995, Chem. Phys., 193, 287
Karpas Z., Anicich V., Huntress W. T., 1979, J. Chem. Phys., 70, 2877
Kim J. h. et al., 2014, ApJS, 210, 14
Kitsionas S., Whitworth A. P., 2002, MNRAS, 330, 129
Kreckel H., Bruhns H., Čížek M., Glover S. C. O., Miller K. A., Urbain X., Savin D. W., 2010, Science, 329, 69
Krstić P. S., Janev R. K., 2003, Phys. Rev. A, 67, 022708
Latif M. A., Volonteri M., 2015, MNRAS, 452, 1026
Latif M. A., Schleicher D. R. G., Schmidt W., Niemeyer J., 2013, MNRAS, 433, 1607
Latif M. A., Bovino S., Van Borm C., Grassi T., Schleicher D. R. G., Spaans M., 2014a, MNRAS, 443, 1979
Latif M. A., Schleicher D. R. G., Bovino S., Grassi T., Spaans M., 2014b, ApJ, 792, 78
Latif M. A., Bovino S., Grassi T., Schleicher D. R. G., Spaans M., 2015, MNRAS, 446, 3163
Lenzuni P., Chernoff D. F., Salpeter E. E., 1991, ApJS, 76, 759
Linder F., Janev R. K., Botero J., 1995, in Janev R. K., ed., Atomic and Molecular Processes in Fusion Edge Plasmas. Plenum Press, New York, p. 397
Martin P. G., Schwarz D. H., Mandy M. E., 1996, ApJ, 461, 265
Matthee J., Sobral D., Santos S., Röttgering H., Darvish B., Mobasher B., 2015, MNRAS, 451, 400
Mayer L., Fiacconi D., Bonoli S., Quinn T., Roškar R., Shen S., Wadsley J., 2015, ApJ, 810, 51
Milosavljević M., Couch S. M., Bromm V., 2009, ApJ, 696, L146
Mirocha J., Skory S., Burns J. O., Wise J. H., 2012, ApJ, 756, 94
Mortlock D. J. et al., 2011, Nature, 474, 616
Oh S. P., Haiman Z., 2002, ApJ, 569, 558
Omukai K., 2000, ApJ, 534, 809
Omukai K., 2001, ApJ, 546, 635
Pallottini A. et al., 2015, MNRAS, 453, 2465
Planck Collaboration XVI, 2014, A&A, 571, A16
Poulaert G., Brouillard F., Claeys W., McGowan J. W., Van Wassenhove G., 1978, J. Phys. B At. Mol. Phys., 11, L671
Regan J. A., Haehnelt M. G., 2009a, MNRAS, 393, 858
Regan J. A., Haehnelt M. G., 2009b, MNRAS, 396, 343
Regan J. A., Johansson P. H., Haehnelt M. G., 2014a, MNRAS, 439, 1160
Regan J. A., Johansson P. H., Wise J. H., 2014b, ApJ, 795, 137 (R14)
Regan J. A., Johansson P. H., Wise J. H., 2015, MNRAS, 449, 3766

Regan J. A., Johansson P. H., Wise J. H., 2016, preprint (arXiv:1603.06612)
Savin D. W., Krstić P. S., Haiman Z., Stancil P. C., 2004, ApJ, 606, L167
Schleicher D. R. G., Palla F., Ferrara A., Galli D., Latif M., 2013, A&A, 558, A59
Schneider I. F., Dulieu O., Giusti-Suzor A., Roueff E., 1994, ApJ, 424, 983
Shang C., Bryan G. L., Haiman Z., 2010, MNRAS, 402, 1249
Sobral D., Matthee J., Darvish B., Schaerer D., Mobasher B., Röttgering H. J. A., Santos S., Hemmati S., 2015, ApJ, 808, 139
Stacy A., Greif T. H., Bromm V., 2010, MNRAS, 403, 45
Stancil P. C., 1994, ApJ, 430, 360
Stecher T. P., Williams D. A., 1967, ApJ, 149, L29
Sugimura K., Omukai K., Inoue A. K., 2014, MNRAS, 445, 544
Tanaka T. L., Li M., 2014, MNRAS, 439, 1092
Tegmark M., Silk J., Rees M. J., Blanchard A., Abel T., Palla F., 1997, ApJ, 474, 1
Tseliakhovich D., Hirata C., 2010, Phys. Rev. D, 82, 083520
Turk M. J., Smith B. D., Oishi J. S., Skory S., Skillman S. W., Abel T., Norman M. L., 2011, ApJS, 192, 9
Venemans B. P. et al., 2013, ApJ, 779, 24
Visbal E., Haiman Z., Bryan G. L., 2014a, MNRAS, 442, L100
Visbal E., Haiman Z., Bryan G. L., 2014b, MNRAS, 445, 1056
Walkauskas L. P., Kaufman F., 1975, Symp. Int. Combust. Proc., 15, 691
Wise J. H., Abel T., 2011, MNRAS, 414, 3458
Wise J. H., Cen R., 2009, ApJ, 693, 984
Wise J. H., Turk M. J., Abel T., 2008, ApJ, 682, 745
Wise J. H., Demchenko V. G., Halicek M. T., Norman M. L., Turk M. J., Abel T., Smith B. D., 2014, MNRAS, 442, 2560
Wishart A. W., 1979, MNRAS, 187, 59p
Wolcott-Green J., Haiman Z., Bryan G. L., 2011, MNRAS, 418, 838
Wu X. B. et al., 2015, Nature, 518, 512

This paper has been typeset from a TEX/LATEX file prepared by the author.